



Universidad
Carlos III de Madrid

SCHOOL OF ENGINEERING

Bioengineering and Aerospace Engineering Department

FINAL DEGREE PROJECT

Experimental Investigation of Horizontal Convection

A Thesis submitted by Lucía Muñoz Córdoba for the degree of
Aerospace Engineering at University Carlos III of Madrid

Supervised by:

Carlos Sanmiguel

Abstract

Fluid circulation driven by buoyancy forces due to a thermal gradient on a horizontal boundary, known as horizontal convection, is experimentally studied. For that purpose, a methacrylate box with inner dimensions $300 \times 150 \times 150 \text{ mm}^3$ (LxWxH) whose bottom is composed by a heat exchanger and a printed circuit board is filled with water. The heat exchanger provides a uniform temperature boundary condition while the printed circuit board provides a boundary condition of uniform heat flux input. The lateral walls and top cover are adiabatic. Moreover, infrared thermography is used together with the heated thin foil sensor technique in order to visualize the results. Experimental set-up components and process to carry the tests are explained in detail. Results are presented as 2D Nusselt number maps, showing three differentiated stages of the transient regime of the fluid circulation and the different results obtained under tested ranges of the boundary conditions ($Ra_F = [1.3 \cdot 10^{11} - 1.1 \cdot 10^{12}]$ at $Pr = 7$ based on initial conditions and aspect ratio of the domain $A = 0.5$). Uncertainties of the results are calculated so that coherent values are ensured. Furthermore, possible future work to be done in this particular thermodynamic-fluid field and conclusions are reported.

Acknowledgements

I would like to specially thank my supervisor Carlos Sanmiguel for all his help and support while working on this final degree project. The technician Carlos Cobos provided a huge help regarding the entire experimental setup; likewise Guillermo Vizcaino concerning the electronic circuit and the infrared camera repair. Moreover, I would also like to thank the Aerospace engineering, Fluid and Structures departments for lending the infrared camera, black body and laboratory where experiments were performed. Finally, to 7.1.H.03 and 7.0.H.05 for providing ideas and different points of view.

Contents

Abstract	i
Acknowledgements	ii
List of Figures	v
List of Tables	vii
Glossary	ix
1 Introduction	1
1.1 State of art	4
1.2 Motivation and objectives	9
2 Heated thin foil sensor technique	10
2.1 External energy contributions	12
2.1.1 Convective heat flux	12
2.1.2 Conductive heat flux	13
2.1.3 Radiative heat flux	14
2.1.4 Heated heat flux	15
2.2 Internal energy evolution	15
2.3 Heat transfer coefficient calculation	16
3 Experimental set-up	17
3.1 Experimental procedure	17
3.2 Experimental layout description	18
3.2.1 Infrared camera characteristics	22
3.2.2 Infrared camera calibration	24
4 Experimental results	31
4.1 Modulation due to printed circuit board	31
4.2 Unsteadiness evaluation	34
4.3 Transient regimes	36
4.3.1 Description of transient regime stages	36
4.3.2 Origin of longitudinal rolls	40
4.4 Rayleigh number study	42
4.5 Evaluation of measured data	46
5 Conclusions	49

A Codes	52
B Project budget	57
Bibliography	60

List of Figures

1.1	Heat transfer modes	2
1.2	Different types of natural convection	2
1.3	Horizontal convection in nature	3
1.4	Cold fluid sinking in oceans	4
1.5	Boundary layer scales	5
1.6	Velocity fields generated by thermal forcing	6
1.7	Horizontal convection with heat flux input	7
1.8	Nusselt number Nu as a function of Ra_F	8
1.9	Studied Rayleigh and Prandtl regimes	8
2.1	System of reference of the box	10
2.2	Infinitesimal heat thin foil element	12
2.3	Convection near the bottom hot surface of a plate	13
2.4	Composition of the printed circuit board	14
3.1	Different perspectives of the experimental layout	17
3.2	Box sketch	19
3.3	Different clamps of the experimental set up	20
3.4	Renault Super 5's radiator and fan assembly	20
3.5	Comparison between a first surface mirror and a regular mirror	21
3.6	Camera and mirror arrangement	21
3.7	Infrared camera SC4000	22
3.8	Aluminum profile structures	23
3.9	Scanning system of an infrared camera	24
3.10	Black body and its power supplier	25
3.11	Intensity level processing	26
3.12	Temperature map processing	27
3.13	Behaviour of the camera with different integration times	28
3.14	Behaviour of the camera with different acquisition frequencies	29
3.15	Behaviour of the camera under experimental set-up	30
4.1	Heat fluxes evolution over time	34
4.2	Unsteady term compared to heat flux due to Joule effect	35
4.3	Initial structures formation, $Ra_F = 5.1 \cdot 10^{11}$	37
4.4	Formation of longitudinal rolls, $Ra_F = 5.1 \cdot 10^{11}$	38
4.5	Fluctuation of longitudinal rolls, $Ra_F = 5.1 \cdot 10^{11}$	39
4.6	Collapse of the longitudinal rolls, $Ra_F = 5.1 \cdot 10^{11}$	40
4.7	Steady regime, $Ra_F = 5.1 \cdot 10^{11}$	41

4.8	Radius of curvature of the printed circuit board	42
4.9	Initial structures comparison, $\tau = 0.41$	43
4.10	Longitudinal rolls development comparison, $\tau = 0.91$	44
4.11	Longitudinal rolls fluctuation comparison, $\tau = 1.55$	44
4.12	Longitudinal rolls collapse comparison, $\tau = 2.02$	45
4.13	Stablished steady regime comparison, $\tau = 6.3$	46

List of Tables

3.1	Infrared camera characteristics	24
3.2	Values of the fitting curve parameters for different integration times	28
3.3	Values of the fitting curve parameters for different acquisition frequencies	29
3.4	Values of the fitting curve parameters for setup behavior	30
4.1	Boundary conditions for each studied case	31
4.2	Biot number comparison	32
4.3	Characteristic times of the phenomenon for each studied case .	33
4.4	Time importance of unsteady term	35
4.5	Non dimensional times for each stage	40
4.6	First transient stage duration	43
4.7	Second transient stage duration	45
4.8	Third transient stage duration	46
4.9	Uncertainty values of h	47
4.10	Uncertainty values of Nu	47
4.11	Uncertainty values of parameters	48
B.1	Cost of materials	57
B.2	Amortization cost	58
B.3	Cost of engineer work	58
B.4	Total project cost	59

Glossary

α	Thermal expansion coefficient	$1/K$
γ^*	Width parameter	
δ_t	Thermal boundary layer thickness	m
δ_v	Velocity boundary layer thickness	m
ϵ	Emissivity coefficient	
ζ	Wall curvature of the printed circuit board	
η	Viscous parameter	
κ	Thermal diffusivity of the printed circuit board	m^2/s
λ_c	Thermal conductivity of copper in-plane	$W/(mK)$
λ_f	Thermal conductivity of fiberglass FR-4 in-plane	$W/(mK)$
μ	Dynamic viscosity	$kg/(ms)$
ν	Kinematic viscosity	m^2/s
ρ_0	Density reference	kg/m^3
ρ_c	Density of copper	kg/m^3
ρ_f	Density of fiberglass FR-4	kg/m^3
ρ_{PCB}	Density of printed circuit board	kg/m^3
σ	Stefan-Boltzmann constant	$W/(m^2K^4)$
τ	Non dimensional time	
A	Aspect Ratio	
A_{PCB}	Surface area of the printed circuit board	m^2
Bi	Biot number	
c_c	Specific heat capacity of copper	$J/(kgK)$
c_f	Specific heat capacity of fiberglass FR-4	$J/(kgK)$
c_{PCB}	Specific heat capacity of the printed circuit board	$J/(kgK)$
E	Radiative energy per unit area	W/m^2
f_{car}	Characteristic frequency of the heat transfer phenomenon	Hz
f_{crit}	Critical frequency of the printed circuit board reaction	Hz
F_0	Fourier number	
F_T	Heat flux per unit area	W/m^2
g	Gravitational constant	m/s^2
G	Görtler number	
h	Convective heat transfer coefficient	$W/(m^2K)$
H	Height of the box	m
I	Intensity	A
k_f	Thermal conductivity of water	$W/(mK)$
k_s	Through-plane thermal conductivity of the printed circuit board	$W/(mK)$

k_{PCB}	In-plane thermal conductivity of the printed circuit board	$W/(mK)$
L	Longitude of the box	m
L_c	Characteristic length of the printed circuit board	m
m	Mass of the printed circuit board	kg
Nu	Nusselt number	
Pr	Prandtl number	
q_a	Convective heat flux per unit area with ambient air	W/m^2
q_{cv}	Convective heat flux per unit area with confined fluid	W/m^2
q_j	Joule effect heat flux per unit area	W/m^2
q_k	Conductive heat flux per unit area	W/m^2
q_{k_x}	Conductive heat flux per unit area along x axis	W/m^2
q_{k_y}	Conductive heat flux per unit area along y axis	W/m^2
q_r	Radiative heat flux per unit area from the printed circuit board	W/m^2
q_R	Radiative heat flux per unit area with ambient air	W/m^2
R	Radius of curvature of the printed circuit board	m
Ra	Rayleigh number	
Ra_F	Rayleigh flux number	
s	Printed circuit board thickness	m
s_c	Copper thickness	m
s_f	Fiberglass FR-4 thickness	m
t_{car}	Characteristic time of the heat transfer phenomenon	s
t_{crit}	Critical time of the printed circuit board reaction	s
T_{amb}	Ambient temperature	K
T_f	Fluid temperature	K
T_w	Wall temperature	K
u	Thermal boundary layer velocity	m/s
v	Thermal boundary layer vertical velocity	m/s
V	Voltage	V
w_c	Copper width	m
w_f	Fiberglass FR-4 width	m
W	Width of the box	m

Chapter 1

Introduction

Heat transfer has always been of scientific interest since as reality shows, it is actually present in many activities and situations. Lots of different technologies are being developed and industries are in need of such knowledge to face up current and future challenges. Some examples of covered engineering fields include alternatives to energy generation, material processing, biotechnology or pharmacology.

Processes in nature are also of interest from a heat transfer point of view: behavior of the atmospheric gases, thermoelectric phenomena, warming of glaciers due to green house effect or volcanism. Particularly, heat transfer in oceans plays a major role when understanding the overturning circulation (thermohaline circulation), as well as behavior of certain species and changes in surface water quality and groundwater characteristics.

Heat transfer is flow of thermal energy between two spatially separated thermal energy levels (temperatures) that goes from the highest to the lowest one. From the second thermodynamic principle three different modes of heat transfer are distinguished: conduction, convection and radiation (Figure 1.1).

- Conduction occurs between adjacent systems or within a stationary medium through direct molecular collisions.
- Convection takes place within a fluid in motion or between a surface and a moving fluid, comprising two mechanisms: random molecular motion from higher to lower concentration regions (diffusion) and bulk, or macroscopic, motion of the fluid (advection).
- Radiation is heat emitted due to changes in the electron configurations of bodies' molecules through electromagnetic waves or photons. In this mode no medium is needed for heat transfer to occur, so that radiative heat transfer is more efficient in vacuum.

Two main types of convective heat transfer are distinguished: natural or free convection and forced convection. In the first one, natural convection, the motion of the fluid is due to buoyancy from density differences by heating itself, that is, it is just present in gravitational fields so that denser fluid sinks and lighter fluid rises. In the second type of convection there are external forces that move the fluid, such as those provided by pumps or fans, for example.

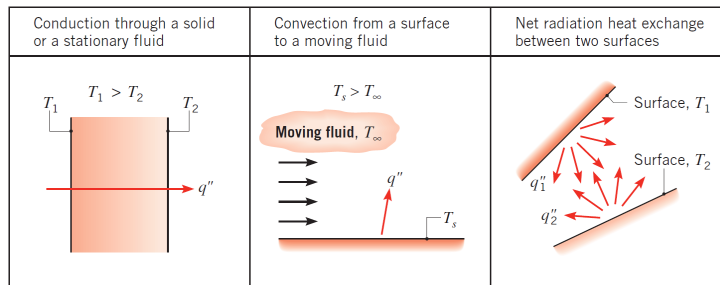


Figure 1.1: Heat transfer modes (Incropera, 2011).

This project is focused on the evolution of a confined fluid driven by buoyancy (natural convection).

The most common and extensively known configuration of natural convection consists on heating a fluid of interest from below and cooling from above, called Rayleigh-Bénard convection, which develops convection cells known as Bénard cells (Figure 1.2(a)). Another similar configuration of natural convection is given by heating and cooling opposite vertical walls of the container of the fluid. The layout of the configuration studied in this project is called horizontal convection, where heating and cooling are both provided from the bottom of the container at the same horizontal level, creating a differential thermal boundary (Figure 1.2(b)).

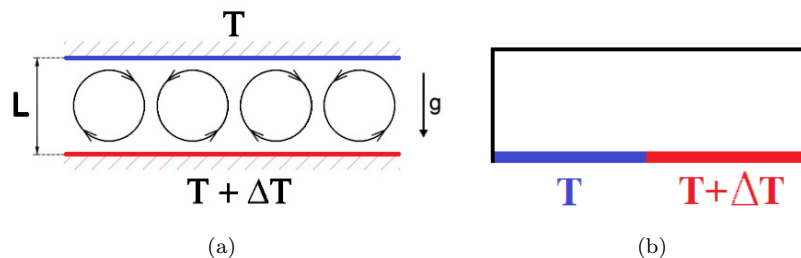
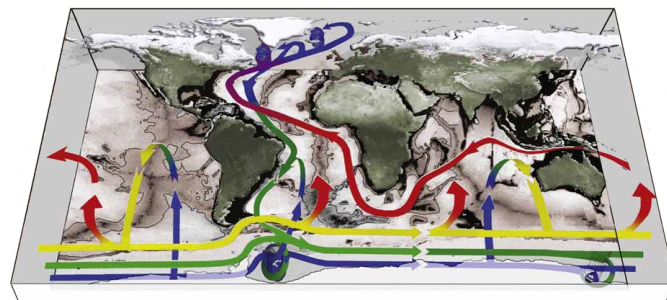


Figure 1.2: Different types of natural convection. 1.2(a) Rayleigh-Bénard convection: at first liquid is in equilibrium but when heating is applied from below, the density of the bottom liquid decreases making it rise while the upper cold liquid sinks (greater density), forming these characteristic Bénard convection cells. 1.2(b) Horizontal convection.

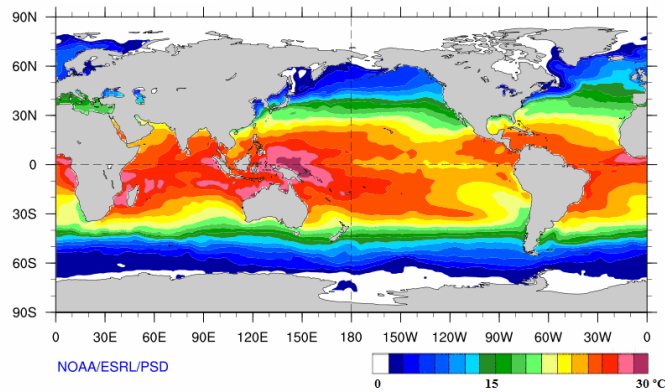
Although horizontal convection is present in many applications nowadays, it has not been studied in depth so far. The interest on this type of convection is increasing thanks to the advantage and usefulness that the understanding and knowledge of this phenomenon can provide to many applications and processes that occur in different industries and nature. As it was mentioned before with heat transfer in general, horizontal convection in particular would also help to understand the dynamics of the meridional overturning circulation of the

oceans (Figure 1.3(a)), since the experimental set-up is nothing more but an upside-down scaled representation of the oceans, considered flat because of their extensions. This way, the cold temperature of the horizontal thermal gradient is considered as it were the North/South Pole meanwhile the hotter temperature represents the Equator (Figure 1.3(b)). Strength and heat transport of the oceans and the influence of surface buoyancy fluxes, such as winds and tides, would be better understood as well.

Because of the scaled configuration, the horizontal approximation is also representative of the atmosphere and the mantle. In the first one, the differential thermal boundary would be similar to that of the oceans, created by the difference in temperature between the Equator and the North/South Pole, but a differential temperature gradient can also be created due to the different in temperature between continents and oceans. In a similar way, for the second case, the presence of continents or oceans above the mantle is what creates the horizontal temperature gradient. Hence, air streams and mantle flows, apart from ocean currents, can be studied for the definition of new, better and faster aerial and navigational routes and for the evolution of lithospheric plates.



(a)



(b)

Figure 1.3: Horizontal convection in nature. 1.3(a) Meridional overturning (Marshall and Speer, 2012) . 1.3(b) Sea Surface Temperature (SST). Cold and hot temperatures are easily appreciated, making up the differential temperature boundary condition of the oceans (NOAA, 2012).

Other applications of horizontal convection are found in industry. Gramberg et al. (2007) and Chiu-Webster et al. (2008) investigated the problem of viscous horizontal convection present in glass furnaces or fired heaters when temperature of the upper surface of the molten glass varies from one end to the other (due to addition of floating cold raw materials at one end and heating by gas flames from above at the other end). On the other hand, there are also patents in the nuclear industry aiming to minimize the effects of horizontal convection in the vessels of nuclear reactors.

1.1 State of art

The earliest experiments dealing with horizontal convection date back to 1908. They were done by Sandström (1908, 1916), using a non-rotating small rectangular box confining a fluid with a system of heating and cooling sources at different levels. He observed that movement in fluids was produced by temperature gradients only if a cooling source was placed higher than a heating source. This statement is known as Sandström’s theorem, which suggests that buoyancy forces alone are not enough to supply energy to the oceanic circulation.

This theorem was accepted by several authors (some of them can be found in Miller (1968)), who ignored the results obtained by Jeffreys. Jeffreys (1925) used a 40.5 cm^3 tank made of Plexiglas to approximate insulating boundaries, and two thermostatically controlled water systems to create the thermal boundary gradient at the bottom. A thermocouple arrangement (sensors that measure temperature) within the fluid helped calculating the heat flow through the fluid. Using this system he proved that “the level of the sources of heat or cold has nothing to do to the motion of the fluid” so that “if there is a temperature gradient the fluid will move”, arguing that Sandström ignored the effects of diffusion. Later, more authors like Hess (1962), Stommel (1962) and Rossby (1965, 1998) proved Sandström’s theorem wrong and agreed with the results obtained by Jeffreys. They also derived interesting results related to oceans, as shown in Figure 1.4.

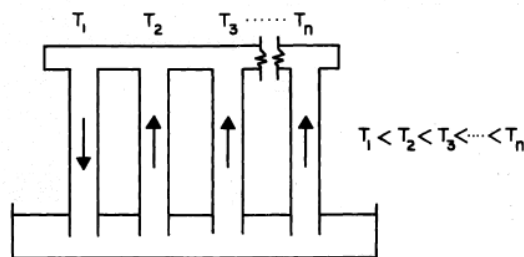


Figure 1.4: Cold fluid sinking in oceans. This phenomenon was firstly explained by Stommel after observing a system of n vertical tubes connected in parallel at their tops by another tube with a non-uniform temperature distribution. The fluid motion of n vertical tubes was upwards in all of them except in the closest to the coldest tube, which was downwards (Miller, 1968).

Among the previous investigators, Rossby stands out because he was the first one developing results for the evolution of the circulation of the fluid and its thermal boundary layer δ_t in horizontal convection. In his case, a uniform horizontal temperature gradient was applied at the bottom of a plexiglass tank ($24.5 \times 7.5 \times 10$ cm) by heating a horizontal aluminum bar at one end and cooling at the other, while the top and side walls were considered non-conducting.

The results he derived are mainly driven by the Rayleigh number Ra , which is a dimensionless relation of natural convection that reflects if heat transfer is primarily in the form of conduction or convection (Equation 1.1, where α is the thermal expansion coefficient of the fluid, g is the gravitational constant, ΔT is the externally applied temperature gradient, L is the longitude of the box where heat transfer takes place, ν is the kinematic viscosity and κ is the thermal diffusivity of the fluid). Nevertheless, unlike Rayleigh-Bénard convection, there is no threshold Rayleigh number for horizontal convection below which convective motion is suppressed (Hughes and Griffiths, 2008). In addition, Prandtl number (relation between momentum diffusivity and thermal diffusivity of the fluid: $Pr = \nu/\kappa$) and the aspect ratio of the domain in which the motion is induced (height H compared to longitude L of the box where the fluid is confined, $A = H/L$) play also a major role in the evolution of the horizontal convection process.

$$Ra = \frac{\alpha g \Delta T L^3}{\nu \kappa} \quad (1.1)$$

In this way, the strength of the stationary circulation and the thermal boundary layer thickness of Rossby's experiments were proved to be proportional to $Ra^{1/5}$ and $Ra^{-1/5}$ respectively, results proved theoretically later in 1998 by the same author. Moreover, he described for the first time three different characteristic thermal boundary layer scales: at the bottom, left wall and top, as it can be seen in Figure 1.5.



Figure 1.5: Zoom in of the left-hand end of the box, showing an asymmetric clockwise circulation occupying the whole depth of the box (Hughes and Griffiths, 2008).

Later in time, Wang and Huang (2005) checked the results obtained by Rossby within four different laboratory experiments under reported accurate conditions (Figure 1.6). Rossby's experiments compromised the thermal isolation of the tank (temperature measurements were taken from an open slot on

the top of the box and the heating source was hotter than the environment) and his experiments did not last more than 10 hours, so that they could have not reached thermal equilibrium. However, Wang and Huang's results agreed that horizontal differential heating always drive a circulation, including cases of heating/cooling from the top or bottom of the tank and at different angles (Figure 1.6). Moreover, they proved the dependence of the thermal boundary layer thickness δ_t to be consistent with $Ra^{-1/5}$, as Rossby did.

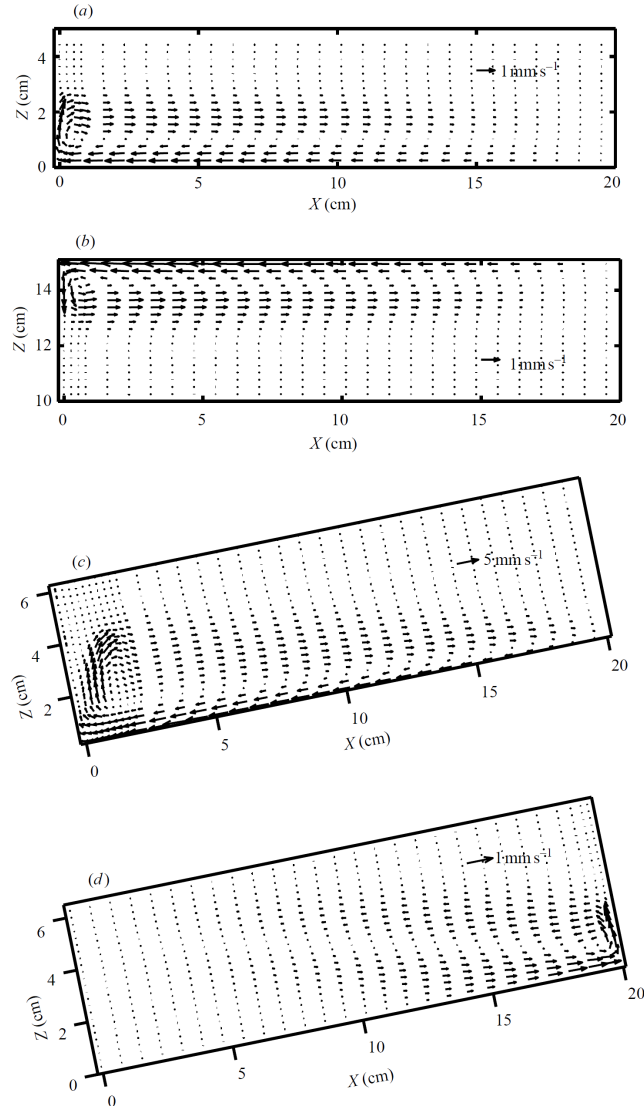


Figure 1.6: Velocity fields generated by thermal forcing: (a), (c) heating at left and cooling at right; (b), (d) heating at right and cooling at left; Bottom is sloping at an angle of 12° in cases (c) and (d) (Wang and Huang, 2005).

Mullarney et al. (2004) introduces a new set up by which horizontal convec-

tion is done. In this set up a thermal boundary layer on the bottom is created by applying a uniform and constant heat flux per unit area F_T [W/m^2] on the heated side ($q=\text{const.}$) and uniform temperature on the other ($T=\text{const.}$). Instead of imposing a temperature gradient on the base, a thermal gradient allows the easy determination and control of the strength of convection and temperature differences (Figure 1.7).

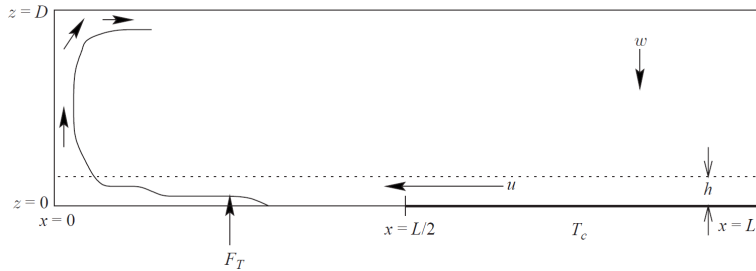


Figure 1.7: Horizontal convection with heat flux input F_T (Mullarney et al., 2004)

In this new set up, the Rayleigh number Ra is redefined to become a Rayleigh number Ra_F based on a heat flux input instead of a thermal gradient (Equation 1.2, where ρ and c_P are the density and the specific heat capacity of the fluid. The subscript $_0$ refers to initial conditions of the confined fluid, i.e.: ambient temperature of $20^\circ C$). Similar to Rossby, Mullarney et al. also developed a numerical solution to the evolution of the Nusselt number ($Nu \sim Ra_F^{1/6}$, Figure 1.8, deeply explained in Section 2), thermal boundary-layer thickness ($\delta_t/L \sim Ra_F^{-1/6}$), thermal boundary-layer velocity ($uL/\kappa \sim Ra_F^{1/6}$) and thermal vertical velocity ($wL/\kappa \sim Ra_F^{1/6}$).

$$Ra_F = \frac{\alpha_0 g F_T L^4}{\nu_0 \kappa_0^2 \rho_0 c_{P0}} \quad (1.2)$$

Every author mentioned before studied the steady behavior of a fluid in a non-rotating setup to better understand the circulation of the oceans. Nevertheless, they did not investigate the rotating horizontal convection that simulates the effect of the rotation of the Earth on the oceans. However, this case was soon reported by many authors, which agreed that consequences of rotation are not important as a first approach (Munk and Wunsch, 1998).

The governing dynamics of horizontal convection have been studied for several differential boundary conditions. A summary of these studies in terms of Prandtl and Rayleigh numbers is shown in Figure 1.9(a), where it can be seen that most studies have been done at high Rayleigh and Prandtl numbers. In Figure 1.9(b) behavior of the flow at different Rayleigh and Prandtl numbers is shown: steady (flow steady and laminar), intrusion (superficial horizontal intrusion beyond the thermal boundary layer) and entrainment (stability thresholds that may be considered unsteadiness) regimes.

There is a discussion regarding the dynamics of horizontal convection: some authors think that this process does not reach a pure turbulent state (Paparella

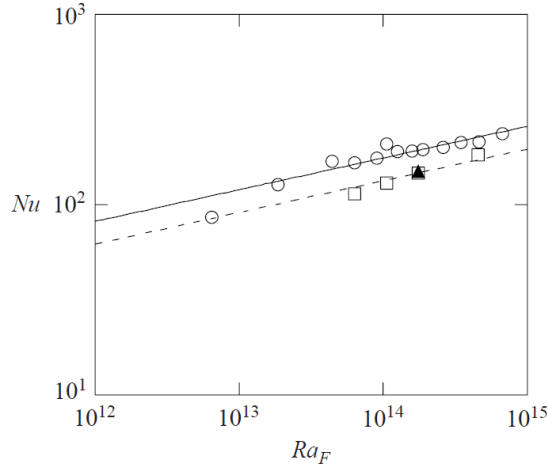


Figure 1.8: Nusselt number Nu as a function of Ra_F . The solid and dashed lines are best fits of the predicted power laws $Nu \sim Ra_F^{1/6}$ to the laboratory data (circles) and numerical data (squares). The solid line is $Nu = 0.82Ra_F^{1/6}$. (Mullarney et al., 2004).

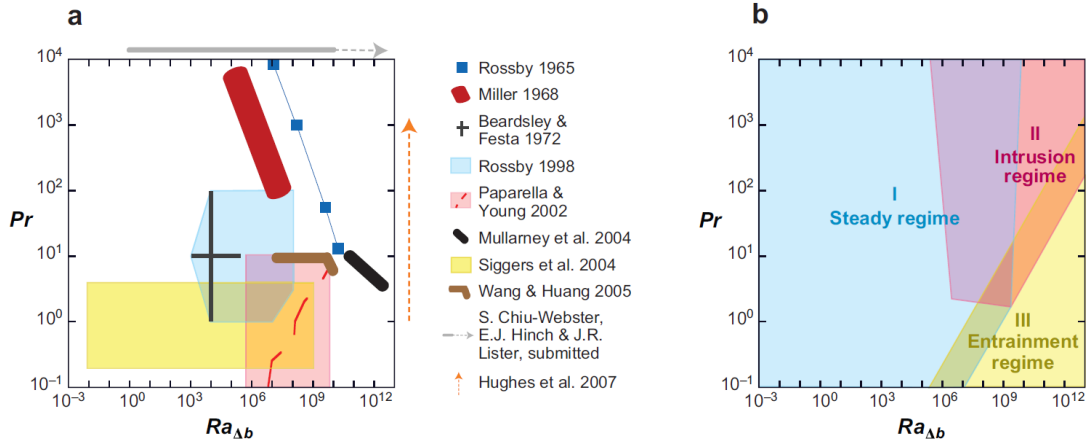


Figure 1.9: Studied Rayleigh and Prandtl regimes (Hughes and Griffiths, 2008).

and Young, 2002) meanwhile some others declare horizontal convection as a turbulent process. At the same time, there is a divided opinion among the authors that declare horizontal convection as a turbulent mechanism: some of them state turbulences are reached thanks to external sources as tidal and wind-driven motion (Huang, 1999, Munk and Wunsch, 1998, Wunsch and Ferrari, 2004), while others support the motion of the flow as just a buoyancy mechanism (Mullarney et al., 2004).

Recently, Gayen et al. (2014) are the authors that have investigated about

horizontal convection the most. They have been using the same experimental layout as Mullarney et al. (2004) in order to focus on the study of the energetics, stability transitions, transient dynamics adjustments and turbulence of horizontal convection (Gayen et al., 2013, 2014, Griffiths et al., 2013).

1.2 Motivation and objectives

Despite of the recent increase of horizontal convection studies, most of them are focused on equilibrium states rather than on transient developments. The previous authors (Griffiths et al., 2013) tested in that “mechanisms of vertical transport are important in [transient] horizontal convection similar to those in previous experiments with equilibrium states (in particular, large Rayleigh number, small aspect ratio and piecewise uniform boundary conditions)”.

In this project the main objective is to study the transient regime of horizontal convection, focusing on the explanation of the three differentiated stages and its behavior under distinct working conditions, that is, the evolution of the fluid at different Rayleigh numbers. However, this main objective implies some more to be accomplished, stated hereinafter:

1. Design and assembly of the experimental set up, considering several alternatives and reasoning the selection of the different elements that finally compose the set up.
2. Start up and refinement of every component, such as a calibration of an infrared camera, before the experiments are carried out.
3. Creation and development of a Matlab code that calculates the heat thin foil behavior under the different conditions the experiments are held.
4. Analysis and comprehension of the practical results, with detailed reasoning and explanation of the observed consequences experienced by the studied fluid.
5. Based on obtained results, suggest new problems or ways to research in this field more deeply.

In the following section the method that studies the fluid heat transfer is explained (Section 2), followed by the description of the experimental setup needed to accomplish such work, as well as its calibration and proper adjustment (Section 3). In the experimental results section (Section 4), the transient regime is observed for several Rayleigh numbers, studying its dependencies. Finally, conclusions are highlighted in the last section (Section 5), providing ideas or work to be done in the future to develop in depth the dependencies and results of this kind of experiments.

The codes used throughout the project are shown in Appendix A, and the total project budget is shown in Appendix B.

Chapter 2

Heated thin foil sensor technique

As it was mentioned before in Section 1 the purpose of these experiments is to study heat transfer within a fluid inside a box (Figure 3.2). This box provides heat to the fluid initially at equilibrium by creating a differential boundary thermal condition through both a heat exchanger that guarantees uniform temperature ($T = \text{const.}$) and a printed circuit board (PCB) that provides a constant heat flux per unit area input ($q = \text{const.}$). The description and functioning of these elements are discussed in detail in following subsections.

Evolution of convective heat transfer in the fluid is measured by the convective heat transfer coefficient h , calculated by means of the heated thin foil sensor technique. Results are presented through the dimensionless Nusselt number Nu , which is the ratio of convection to conduction heat transfer normal to the bottom surface of the box. Nusselt numbers close to one mean that convection and conduction are of similar magnitude, characteristic of laminar flow, while larger Nusselt numbers correspond to more active convection, with turbulent flow usually in the 100–1000 range.

Convective and conductive heat transfers are measured by convective and

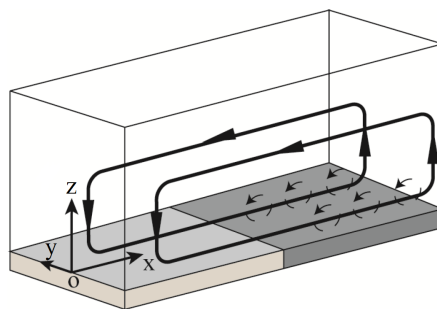


Figure 2.1: System of reference of the box. The printed circuit board is placed in the dark gray area while the heat exchanger is placed in the light gray area (Ceglia et al., 2012).

conductive heat fluxes, which are energy per unit surface and per unit time (W/m^2). Heat flux is determined by Newton's cooling law that states that heat flux per unit area q'' is nearly proportional to the temperature difference $T_w - T_x$, where T_w is the temperature of the body's surface and T_x is the temperature where heat flux is needed to be calculated.

As a general convention q'' is used as heat flux per unit area and Q is heat flux of the entire body or element in question. However, q is used in this project as heat flux per unit area for simplification. Moreover, it is noted that heat flux q'' is a vector (see Figure 1.1) but in this project heat fluxes are treated as constants, so that the vectorial sense is implemented in their modulus.

For convection to occur, a fluid layer of width L and temperature difference ($T_w - T_x$) has to be moving so that convective heat flux is $q_{cv} = h(T_w - T_x)$, where h is the convective heat transfer coefficient between the fluid and the wall.

If, on the other hand, the layer is stagnant, heat flux would be entirely due to fluid conduction through the layer: $q_k = k_f(T_w - T_x)/L$, where k_f is the thermal conductivity of the fluid. As previously mentioned, the fluid used in these experiments is water, which has a thermal conductivity $k_f = 0.6 W/(Km)$ at $20^\circ C$.

In this way, the Nusselt number ends up being defined as

$$Nu = \frac{\text{Convective heat transfer}}{\text{Conductive heat transfer}} = \frac{hL}{k_f} \quad (2.1)$$

where L is the characteristic length where heat transfer occurs, which in this case is the whole length of the box ($L = 0.3m$).

From previous expression every term of the equation is known but the convective heat transfer coefficient h . In the experiments this coefficient relates heat flux per unit temperature difference between the fluid and the electric circuit. Since fluid data cannot be calculated because of complexity, this coefficient is then calculated focusing on the energy balance of the printed circuit board and observing the XY plane where the printed circuit board is placed (Figure 2.1).

In order to calculate the energy balance between the internal and the external energy of the printed circuit board every external energy term involved in the PCB is considered. Since the balance is calculated within an infinitesimal element of the PCB the energy terms used are heat fluxes. These external energy terms are: heating of the printed circuit board by Joule effect q_j , conduction within the PCB q_k , convection with the fluid q_{cv} , convection with the ambient q_a , radiation from the PCB q_R and radiation from the ambient to the PCB q_r , as it can be seen in Figure 2.2.

The walls of the box are considered to be adiabatic, and thus conduction between them and the printed circuit board is zero. The surface of the PCB in contact with the fluid is called the front surface, while the opposite one is called the back surface. The Biot number Bi relates the internal diffusion resistance to the external convection resistance no dimensionally ($Bi = \frac{hs}{k_s}$), determining very small internal temperature gradients along the PCB thickness (explained in detail in 4.1) so that temperatures at front and back surfaces are assumed to be the same (T_w). This way, the PCB is considered a thin foil, being able to observe the evolution of the fluid just evaluating the back surface of the PCB, and giving in addition the name to this method: heated thin foil method.

The previous external energy contributions are compared to the internal thermal evolution of the printed circuit board in order to account for its energy

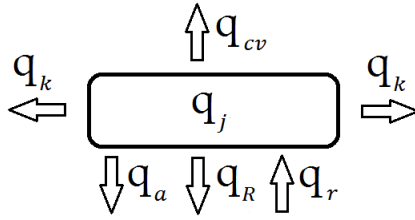


Figure 2.2: Infinitesimal heat thin foil element showing every external energy term acting on it.

balance:

$$\frac{m c_{PCB}}{A_{PCB}} \frac{\partial T}{\partial t} = -q_a - q_k - q_{cv} - q_R + q_r + q_j \quad (2.2)$$

where m is the mass of the PCB and A_{PCB} and c_{PCB} are its area and specific heat capacity, respectively. It is noted that the calculation of both energy contributions (external and internal) are considered to be per unit area.

2.1 External energy contributions

The calculation of the different external and internal heat fluxes is explained in the following subsections, for which the adopted sign convention is such that is positive when energy goes into the printed circuit board and negative when it is released by the printed circuit board.

2.1.1 Convective heat flux

As it was mentioned above, two convective heat fluxes are differentiated: convection between the printed circuit board and the confined fluid q_{cv} and convection between the printed circuit board and the surrounding air q_a .

The first one, q_{cv} , is calculated as explained before thanks to Newton's cooling law (Equation 2.3), where h is the convective heat transfer coefficient the heated thin foil method is going to solve, T_w is the temperature of the PCB and T_f is the temperature of the fluid.

$$q_{cv} = h(T_w - T_f) \quad (2.3)$$

As it will be explained in the experimental procedure, Section 3.1, T_w is acquired by means of an infrared camera while T_f is the temperature of the fluid. This last temperature T_f is the temperature of the fluid next to the front surface of the PCB. Unlikely, no method is available in these experiments to measure this temperature, but previous studies have shown that this temperature is the same as the average interior fluid one (Mullarney et al., 2004). During stationary developments the heat flux rate applied to the water is the same as the one extracted by the heat exchanger, therefore interior fluid temperature remains constant and equal to the ambient temperature T_{amb} . This way, fluid temperature T_f is considered to be equal to ambient temperature T_{amb} .

On the other hand, according to Incropera (2011) convection heat flux with the ambient air q_a is usually neglected (Equation 2.4): “A hot surface facing downward (Figure 2.3), the tendency of the fluid to descend and ascend, respectively, is impeded by the plate. The flow must move horizontally before it can descend or ascend from the edges of the plate, and convection heat transfer is somewhat ineffective.”

$$q_a \approx 0 \quad (2.4)$$

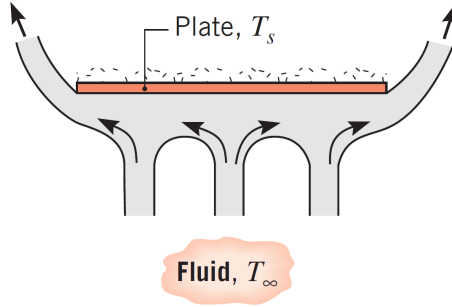


Figure 2.3: Convection near the bottom hot surface of a plate. Tendency of fluid motion due to convection near the bottom hot surface of a plate when $T_s > T_\infty$ (Incropera, 2011).

2.1.2 Conductive heat flux

As it can be seen in Figure 2.2 conductive heat flux q_k is present within the printed circuit board. In principle, it is calculated as it was explained before for the Nusselt number: $q_k = k_{PCB}(T_w - T_x)/L$, where k_{PCB} is the in-plane thermal conductivity of the PCB. Nevertheless, the calculation of k_{PCB} is not straightforward due to the geometry and the different materials that compose the board (Figure 2.4).

In order to do so, a cartesian coordinate system allows the calculation of the conductive heat flux splitting the conduction in the directions normal and parallel to the copper tracks (Astarita et al., 2006). Therefore, the total conductive heat flux is the sum of the heat fluxes along the x and y directions, as shown in Equation 2.5.

$$q_k = q_{k_x} + q_{k_y} \quad (2.5)$$

Along the y-axis, the conductive heat flux is the sum of two mechanisms in parallel, one due to the copper tracks and the other one to the fiberglass support, finally obtaining:

$$q_{k_y} = - \left(\frac{w_c s_c \lambda_c + w_f s_f \lambda_f}{w_f} \right) \frac{\partial^2 T}{\partial y^2} = - (\gamma * s_c \lambda_c + w_f s_f) \frac{\partial^2 T}{\partial y^2} \quad (2.6)$$

where w indicates width; s thickness; the suffixes c and f are relative to copper and to fiberglass FR-4, respectively, and it has been introduced the width

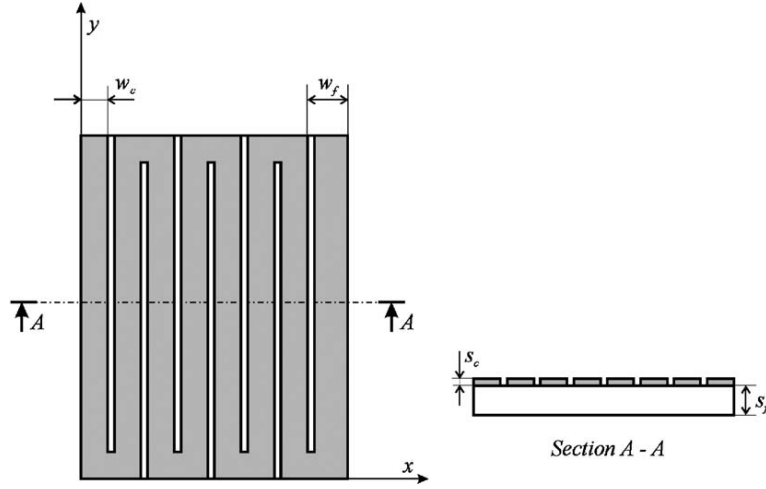


Figure 2.4: Composition of the printed circuit board: fiberglass FR-4 is shown in white while copper is shown in dark gray (Astarita et al., 2006).

parameter γ^* defined as $\gamma^* = w_c/w_f$. λ refers to the conductive coefficient of each material.

However, the calculation of heat flux is slightly more complicated in the direction normal to the copper tracks. In the copper gap only fiberglass allows conductive heat transfer while, in the track zone, both materials contribute to it. Therefore, in this case, the conductive heat transfer can be estimated as due to both a series and a parallel processes:

$$q_{k_x} = - \left(\frac{1 - \gamma^*}{s_f w_f} + \frac{\gamma^*}{s_c w_c + s_f w_f} \right) \frac{\partial^2 T}{\partial x^2} \quad (2.7)$$

2.1.3 Radiative heat flux

Radiative heat flux is measured by Stefan–Boltzmann law, for which radiation energy is proportional to the temperature of the surface of the body: $E = \epsilon \sigma T^4$ where σ is the Stefan–Boltzmann constant ($\sigma = 5.67 \cdot 10^{-8} \text{ W}/(\text{m}^2 \text{K}^4)$), ϵ is the total emissivity coefficient, and T is the temperature of the studied body. The emissivity coefficient ϵ quantifies the level of radiation emitted by a material, ranging between 0 and 1, so that the higher the value the higher the rate at which radiation is transmitted.

Hence, taking into account radiation going to the PCB from the surrounding ambient q_r and radiation coming from the PCB to the ambient q_R the final expressions would result to be: $q_r = \epsilon \sigma (T_{amb})^4$ and $q_R = -\epsilon \sigma (T_w)^4$, so that T_w and T_{amb} are the temperature of the PCB's back surface and of the surrounding ambient, respectively.

$$q_{r-R} = \epsilon \sigma (T_{amb}^4 - T_w^4) \quad (2.8)$$

The back surface of the printed circuit board is externally coated with a thin layer of high emissivity paint (emissivity coefficient $\epsilon = 0.95$) in order to

improve the signal to noise ratio of the IR camera system, that is, improve the sensitivity of the camera to the this emitted light. The final expression of the radiation terms may be expressed as Equation 2.8, since both terms are emitted from the PCB surface and so they have the same emissivity coefficient ϵ . This way, the PCB back surface radiates energy to an infrared (IR) camera, finally obtaining a 2D temperature map of the PBC surface. The characteristics and functioning of the camera are explained later in Section 3.2.1 and Section 3.2.2.

Since the obtained temperature field is a 2D map, it has to be pointed out that the heat transfer coefficient is not a constant value but varies within the PCB surface, as the temperature field does.

2.1.4 Heated heat flux

The printed circuit board is heated up thanks to Joule's first law, which states that electric current passing through a conductor releases heat. Therefore, Equation 2.9 shows heat flux is proportional to the current I that passes through the circuit and the voltage V across the same divided by the total area of the PCB. Joule effect enables a quasi-spatially constant heating within the PCB (Astarita et al., 2006).

$$q_j = \frac{VI}{A_{PCB}} \quad (2.9)$$

Both the intensity and voltage of the electric circuit are measured at the same time the experiments are carried out. The use of adjustable power supplier allows to work within different conditions and a wide range of Rayleigh numbers, calculated as Equation 1.2 shows. The Rayleigh flux number Ra_F is proportional to the applied heat flux F_T , which is the addition of all the heat fluxes applied to the confined fluid. According to Mullarney et al. (2004) it is equal to the heat flux added due to Joule effect by the printed circuit board (q_j). This way, the Rayleigh flux number Ra_F is finally defined as in Equation 2.10 that shows the dependence of this ratio to the voltage of the circuit to be directly proportional.

$$Ra_F = \frac{\alpha_0 g q_j L^4}{\nu_0 \rho_0 c_{P0} \kappa_0^2} \quad (2.10)$$

2.2 Internal energy evolution

The infinitesimal internal energy evolution of the PCB is reflected by the left hand term of Equation 2.2, where c_{PCB} and m are calculated through volume ratios regarding the distribution of FR-4 and copper. This way:

$$c_{PCB} = \frac{c_c s_c w_c + c_f s_f w_f}{s_c w_c + s_f w_f} \quad (2.11)$$

$$m = \rho_c s_c w_c l_c l_f + \rho_f s_f l_f^2 \quad (2.12)$$

where l_f is the length along the y-axis (the same for copper and FR-4) and l_c is the length of copper along the x-axis. Since the PCB is a square, and as it can be seen in Figure 2.4, the length of FR-4 along the x-axis is the same one as along the y-axis.

2.3 Heat transfer coefficient calculation

After the definition of every heat transfer flux and the internal energy term, the energy balance expression turns out to finally be:

$$\frac{mc_{PCB}}{A_{PCB}} \frac{\partial T}{\partial t} = -h(T_w - T_f) + \epsilon\sigma(T_{amb}^4 - T_w^4) - q_{k_x} - q_{k_y} + \frac{VI}{A_{PCB}} \quad (2.13)$$

where q_{k_x} and q_{k_y} were defined in Equations 2.7 and 2.6 respectively, easily obtaining the convective heat transfer coefficient h :

$$h = \frac{-q_{k_x} - q_{k_y} + \frac{VI}{A_{PCB}} + \epsilon\sigma(T_{amb}^4 - T_w^4) - \frac{mc_{PCB}}{A_{PCB}} \frac{\partial T}{\partial t}}{(T_w - T_f)} \quad (2.14)$$

As it was mentioned in the definition of the different heat fluxes, T_{amb}, T_f are measured the day of the experiments, being T_w the only one left to be evaluated, which is done by means of the infrared camera.

In the experimental results (Section 4) the calculation of this coefficient, as well as the transient development of the convection heat transfer and some of its dependencies by means of the Nusselt number (Equation 2.1) are shown and explained in detail. However, the experimental set up description needed to achieve results is firstly shown in the next section.

Chapter 3

Experimental set-up

In this chapter the experimental set up is described in detail. First of all, the entire working of the set up is explained to later discuss the elements that compose it. It is of interest that the working, processing and calibration of the infrared camera are also commented.

3.1 Experimental procedure

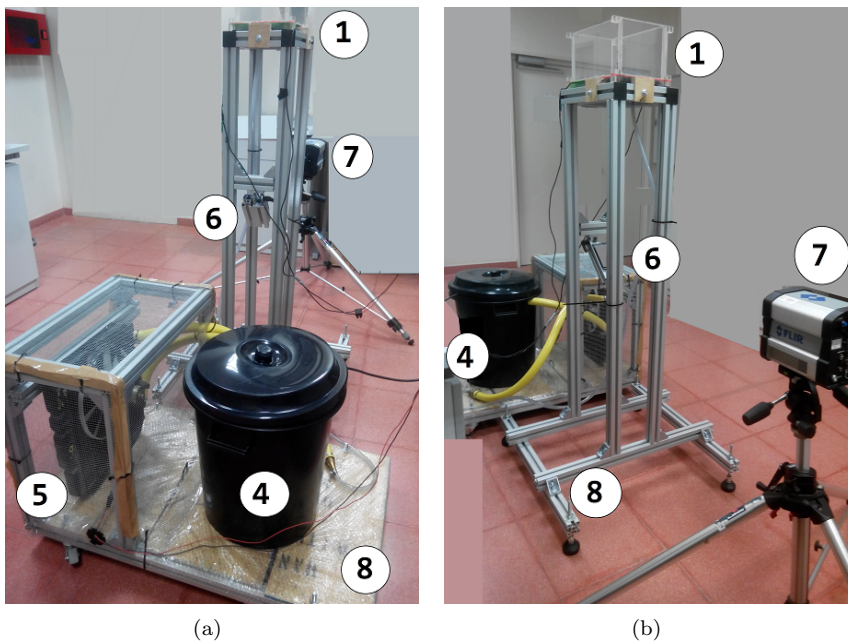


Figure 3.1: Different perspectives of the experimental layout.

The real experimental set up is shown in Figure 3.1. Experiments are carried out in an insulated box (1) whose base is divided in two halves: one holds a

heat exchanger (2) and the other holds a printed circuit board (3). Water is pumped (4) to the heat exchanger and maintained at ambient temperature by a water radiator-fan assembly (5) while the printed circuit board (PCB) is heated up by means of Joule effect. A first surface mirror (6) and an infrared camera (7) collect the data coming from the printed circuit board. Meanwhile, different structures of aluminum profiles (8) keep the box, the radiator-fan assembly and the pump fixed.

The experimental procedure starts by filling the box with water and let it rest for several days in order to degas it and get rid of the possible formation of bubbles. After that, a constant water temperature has to be reached inside the insulated box, so the heat exchanger water circuit is turned on several hours before carrying out the tests. Initially, water inside a water bucket is pumped to the heat exchanger circuit of the box going through a water radiator-fan assembly. The water inside the bucket is at constant temperature (ambient temperature) and the high conductivity of the heat exchanger, which is made of copper, is able to transmit this temperature to the water inside the box.

Radiator-fan assembly ensures water temperature of the water circuit is maintained at a constant ambient temperature during the experiments, so that this system is also turned on before the experiments are taken.

Once a constant temperature is reached inside the box, the electric circuit made by the printed circuit board is switched on. Right before, the camera is also turned on so that the flow visualization initiates at the same time the electrical circuit starts working. A first surface mirror is placed below the electrical circuit to reflect the image to the camera at 45 degrees.

Later on, the data received by the camera is processed in order to observe and study the heat transfer evolution of the fluid.

3.2 Experimental layout description

Characteristics of the different components mentioned above are described hereafter, whose costs are specified in Appendix B. Several options have been considered for each component of the experimental set up but hereinafter the chosen ones are detailed, just mentioning some of the most important alternatives. In addition, preventive measures have been taken to avert any risk, in agreement with Protection of labor data law.

1. The box is made of Plexiglas GS 233 with longitude $L = 300mm$, width $W = 150mm$ and height $H = 150mm$ as inner dimensions. A wall thickness of 15 mm ensures the thermal insulation of the lateral walls, minimizing the conductive thermal losses tangentially and with the exterior. The top cover is also 15mm to meet the same requirement (Figure 3.2). No other alternatives to the box have been considered because this assembly was already built and it was the starting point for the rest of the assembly, therefore, no alternatives for the heat exchanger or the printed circuit board were considered either. However, based on experience, advisable improvements of this box assembly are suggested in Section 5.
2. The heat exchanger is made of a serpentine copper tube silver-soldered to a 10mm thick electrolytic copper plate (15cm long, 15cm wide), shown in

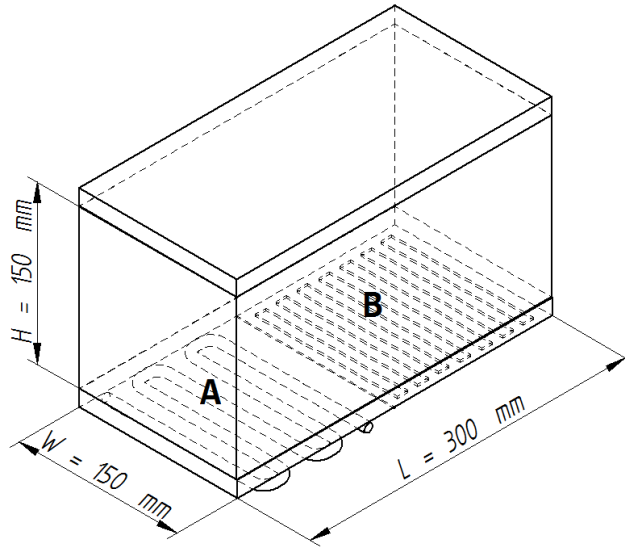


Figure 3.2: Box sketch. Placements of the heat exchanger (A) and the printed circuit board (B) are shown.

area A of Figure 3.2. The high thermal conductivity of the plate (approximately $k_{PCB} = 401 \text{ W/(mK)}$) guarantees the desired boundary condition of uniform temperature ($T = \text{const.}$).

3. The printed circuit board is shown in area B of the representation of the box (Figure 3.2). Its copper tracks are $5\mu\text{m}$ thick, 1.8mm wide and placed at a 2mm pitch. The total board thickness, including the fiberglass layer, is 0.5mm . A 1mm thick support rod reduces the effect of deflection of the printed circuit board due to hydrostatic pressure, shown in results as a black rectangle. The circuit in-plane dimensions are $150 \times 150 \text{ mm}^2$, providing the uniform heat flux input boundary condition ($q = \text{const.}$). These dimensions are well defined in Figure 2.4.

This circuit makes use of a variable power supplier of maximum output voltage of 35V and current limit of 5A , so that voltage and intensity of the circuit can be varied, thus also varying the working conditions of the experiments. As it was shown in the previous chapter, q_j is then varied and so the heat transfer convection h and the Nusselt number Nu (Section 2.1.4).

4. Water of the heat exchanger circuit is drew up by a pump placed from a bucket filled with water to the heat exchanger of the box. Its maximum head pump size is 5m (maximum height to which the pump lifts water) and its maximum flow rate is 125l/min . Although water is needed to go up about 2 meters, greater head pump was chosen so that there are no load losses with narrowing of the circuit. It is connected directly to Direct Current (DC), working at 230V in order to pump the water to the heat exchanger after passing through the radiator-fan assembly.



Figure 3.3: Different clamps of the experimental set up. 3.3(a) Radiator and fan assembly clamp. 3.3(b) Heat exchanger clamp.

Clamps throughout the circuit ensure there are no liquid losses in any of the connections among the pump, the radiator-fan assembly and the heat exchanger tubes (Figure 3.3(a) and Figure 3.3(b)). Since the diameter of the radiator-fan assembly's hoses are much greater than the tubes entering the heat exchanger of the box, a reduction of diameter of hoses is needed (Figure 3.3(a)).

5. An already built Renault Super 5's radiator-fan assembly (Figure 5) is used to maintain the water circuit at constant temperature. The fan works connected to a fixed power supplier of 12V and 120W. However, this circuit needs to use a varistor or voltage-dependent resistor (VDR) placed in parallel as a control element in the electrical circuit to protect the fan against excessive transient voltages. Its electrical resistivity varies inversely proportional to the applied voltage so that at low voltage it has a high electrical resistance that decreases as the voltage is raised.

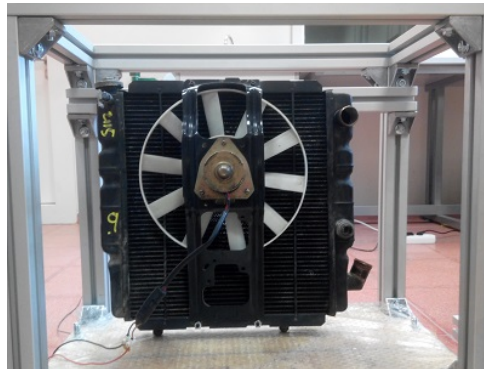


Figure 3.4: Renault Super 5's radiator and fan assembly placed in the aluminum profiles.

6. A first surface mirror or front surface mirror (commonly abbreviated as FS mirror or FSM) is used to reflect the radiation from the PCB and be

able to place the infrared camera horizontally. It minimizes energy loss by not allowing light to pass through the glass substrate by means of an aluminum coating on the face of the glass (against regular mirrors that it is applied on the backside of the glass creating a faint secondary reflection as shown in Figure 3.5). Thus, the amount of light reflected is maximized and distortion is minimized.

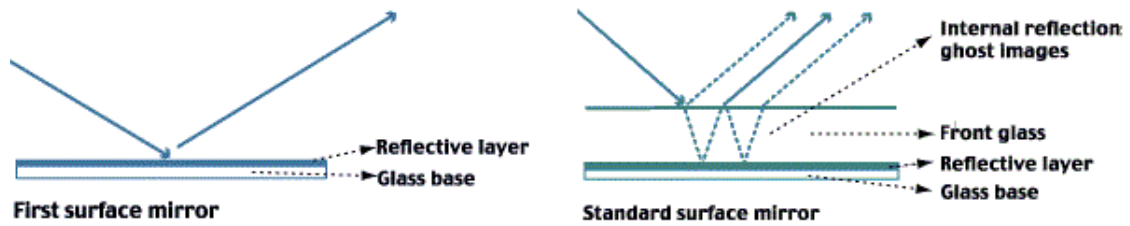


Figure 3.5: Comparison between a first surface mirror and a regular mirror (fsm, 2015).

This mirror (shown in Figure 3.6(a)) is used in order to not place the infrared camera just below the box of the experiments, so that in case the box falls down, the camera is not damaged (Figure 3.6(b)). Besides, it would be complicated to build a structure that fixes the camera vertically.

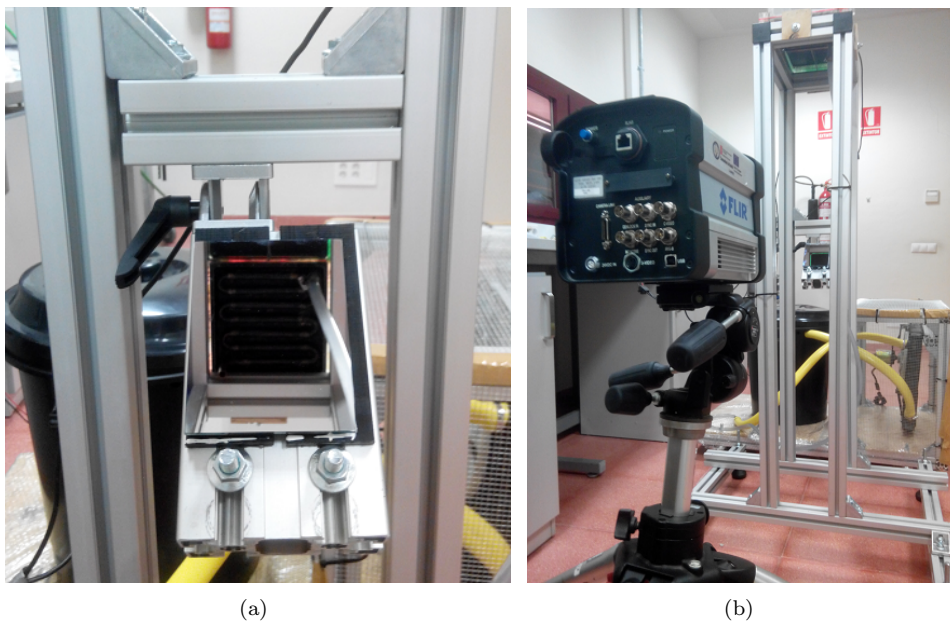


Figure 3.6: Camera and mirror arrangement: 3.6(a) Close-up of the FS mirror, 3.6(b) The infrared camera is not placed below the box.

7. The thermal infrared camera (IR camera) shown in Figure 3.7 is used to

observe the radiative heat transfer evolution of the printed circuit board. This type of cameras acquires data from a range of radiation wavelengths longer than those of visible light (nominal visible light extends from $700\mu m$ to $1mm$ while infrared range extends from $0.75\mu m$ to $15\mu m$). Its function and characteristics are deeply explained in Section 3.2.1 and Section 3.2.2, since its calibration and operation are crucial to obtain understandable and reasonable temperature results. It was borrowed from another department of the university, so no other alternatives were deeply considered.



Figure 3.7: Infrared camera SC4000 (Flir, 2008).

8. Fasten aluminum profiles maintain the box placed at certain altitude (at about 1.6 m) providing an easy and comfortable way to handle it while experiments are taking place (Figure 3.1(a)). The first surface mirror is also sustained by a mobile surface profile so that the direction of the reflected radiation from the infrared camera is simple to change. For that purpose, an horizontal profile adjusts the altitude while a handle (shown at the left in Figure 3.6(a)) ables to change the angle at which the mirror is placed.

The bucket for the water and the Renault super 5 radiator-fan assembly are also placed on a profile assembly (Figure 3.8(a) and Figure 3.8(b)). This structure is separated from the profile one of the box in order to provide more security to the experiments. As it can be seen in the pictures, wheels are implemented to create an easily mobile structure that can be placed where needed without interrupt the evolution of the experiments. Moreover, to avoid any possible damage with the fan, a wire mesh is attached to the structure.

At first, placing all together (the bucket, the radiator-fan assembly and the box) was considered but instabilities and vibrations of the fan and pump would have been transmitted through the structure to the box, making the experiments to fail. In order to remove vibrations on the profile assembly of the box, vibration absorbers have been used (Figure 3.8(c)).

3.2.1 Infrared camera characteristics

Within the experiments of this project a thermal infrared camera is used to observe the heat transfer evolution of a fluid through a printed circuit board. Specifically, the camera is in charge of record the evolution of the PCB back

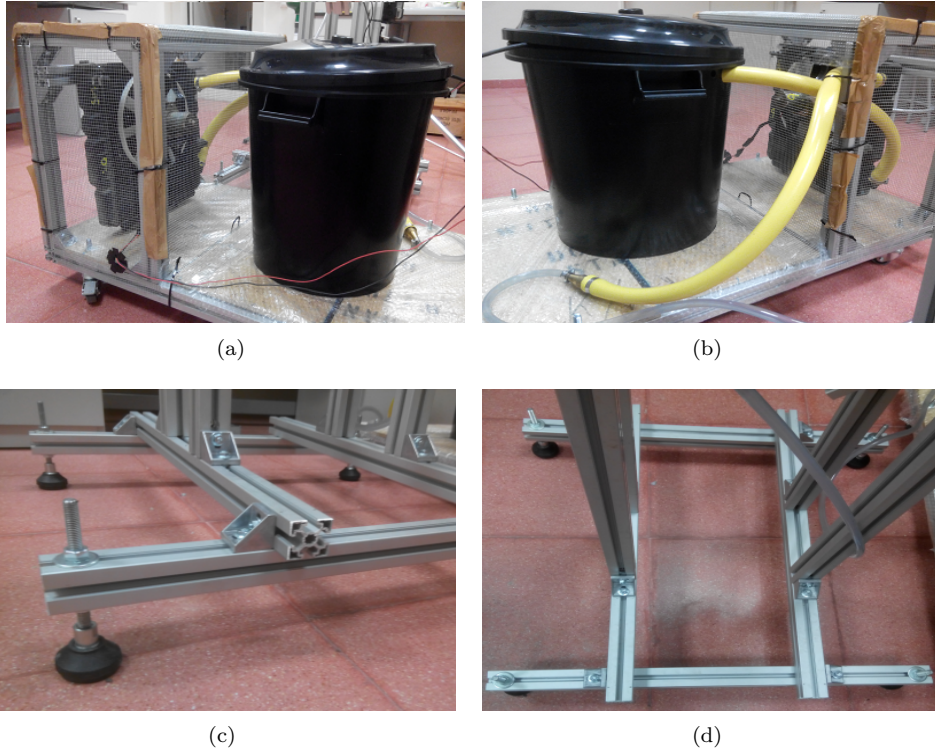


Figure 3.8: Aluminum profile structures: 3.8(a) Left-side view of the mobile structure, 3.8(b) Right-side view of the mobile structure, 3.8(c) Vibration absorbers of the box structure, 3.8(d) Base profile of the box structure.

surface temperature, T_w . This camera uses an infrared scanning radiometer system that receives the thermal radiation emitted by the PCB to finally generate a temperature map. The components involved in this system are an optical system, an infrared temperature detector, a frame grabber and a process unit, as shown in Figure 3.9.

The optical system consists on a series of lens and transparent mirrors (i.e.: made with high refractive index materials) that collects and deflects the emitted radiation to the temperature detector, which is sensible to the selected infrared band. In case the selected infrared band is not supported by the temperature detector, filters or coatings can be used in the lens so that the range of temperatures of the detector is covered. The temperature detector converts the impinging radiation into an electrical signal by a photon detector that excites electrons and changes their energy (or quantum) level. Better results are obtained if the temperature of the temperature detector is decreased by means of a cooling system placed right next to it (they are usually assembled together). Once the electrical signal is created, it is addressed by an electronic processor that conditions that signal and converts it to A/C so that it is perfectly readable by certain PC software, Flir Tools Software in this case. In order to do so, a calibration is needed to match the produced electrical signal with the real viewed temperature.

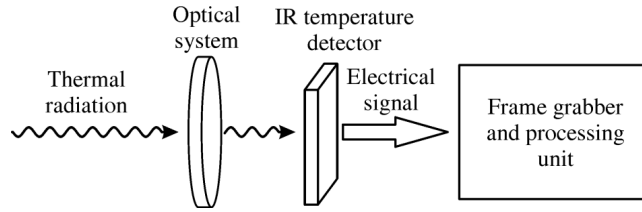


Figure 3.9: Scanning system of an infrared camera (Astarita and Carlomagno, 2012)

The thermal infrared camera (or IR camera) used in these experiments is Flir SC 4000 MWIR (Figure 3.7), whose performance is driven by thermal sensitivity, spatial resolution and acquisition frequency as well as temperature and dynamic ranges. Its characteristics are shown in Table 3.1.

Characteristic	Definition	Measured by	Value
Thermal sensitivity	Time standard deviation of the random background noise averaged over all pixels of a black body scene	Noise Equivalent Temperature Difference (NETD)	<18 mK
Spatial resolution	Capability to resolve temperature differences between points placed at relatively small distances	Pixels x pixels	320x256 pixels (Horizontal x Vertical)
Spectral range	Range of wavelengths the camera is able to work in	Distance	1.5-5 μm (broadband option)
Acquisition frequency	Full frames acquired per second	Frequency	0.1-432 Hz
Temperature range	Range of temperatures the camera is able to work in	Temperature	-20 up to +1500 $^{\circ}\text{C}$ (without filters)
Dynamic range	Number of digital intensity levels the individual pixel signal is composed of	Bits of data	14 bits

Table 3.1: Infrared camera characteristics (Flir, 2008)

The range of temperatures at which the camera is exposed in these experiments is $18 - 90^{\circ}\text{C}$ because of the calibration process, but generally the temperature is maintain at ambient temperature (20°C).

3.2.2 Infrared camera calibration

As mentioned before, a proper calibration of the IR camera is needed to match correctly the real temperature profile with the received electrical signal by means of a function (with constants to be determined). This process is not straight-

forward because there are many exterior contributions to the studied fluid that influence the radiation received by the camera either by attenuating or increasing it. Some of these contributions are the ambient environment (known or changing temperature), the atmosphere or even the radiation of the thermal infrared camera itself.

The calibration makes use of a black body, also known as a perfect emitter and absorber of radiation, which is an opaque material that reflects all the received incident radiation in many directions. As mentioned in Section 2.1.3, the level of radiation emitted by a material is quantified by an emissivity coefficient ϵ that ranges between 0 and 1, so that the higher the value the higher the rate at which radiation is transmitted (i.e.: for a black body, $\epsilon = 1$). The calibration process consists on ranging the temperature of a black body in the field of study (20-80 °C in this project) and matching the results with the energy level of the electrons displayed by the output signal of the camera (given by intensity numbers).



Figure 3.10: Black body (1) and its power supplier (2). Courtesy of Structures Department (UC3M).

To begin with, the ambient temperature at which the calibration is performed is taken at the beginning and at the end of the process to ensure ambient temperature is similar to the one at which experiments are done and that it does not change abruptly within the calibration process. If a significant difference of temperature is observed the calibration would be discarded because the results would be distorted.

Once the camera is properly connected to the computer and the software is able to read it, a correction to what the pixels of the camera read is done because not every pixel reads the same temperature. This is due to their different proximities to the frame (i.e.: the nearer to the frame the colder the read temperature) and their different sensitivities (errors regarding production of each pixel). For this purpose, a surface of constant temperature is placed right in front of the camera so it automatically readjusts the temperature each pixel should read.

Afterwards, the focal length of the camera is adjusted in order to focus the black body accurately from the distance the camera is placed. For this purpose, a metal object with inscriptions on it (in this case, a key) is used: it is placed right ahead of the black body, and the high emissivity of the metal allows the quick focus of the image.

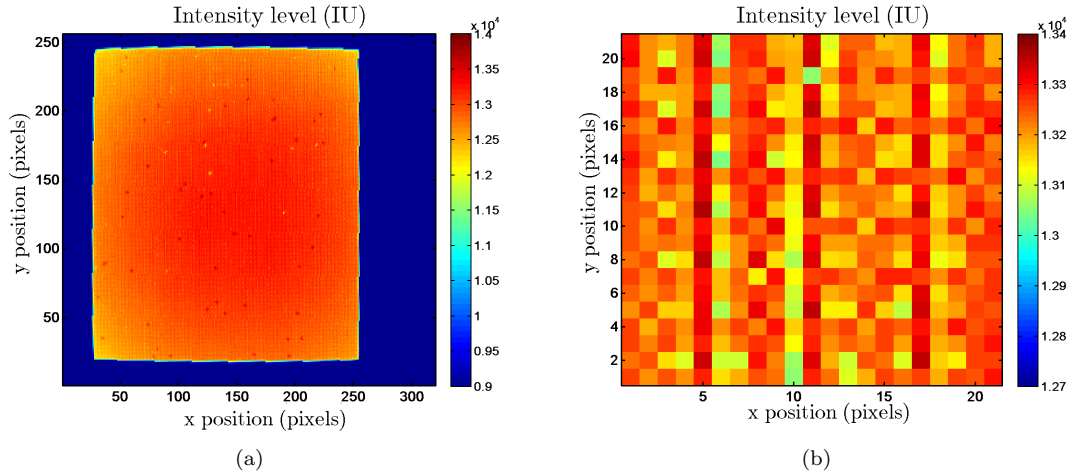


Figure 3.11: Intensity level processing: First of all, a set of data is analyzed and treated as an image (3.11(a)). The area of interest of images is considered in following data processing. For calibrations, this area is a set of 20x20 pixels, showing a variation of 200 intensity units for a constant temperature (3.11(b)). However, this intensity levels are later translated to temperatures thanks to the calculated calibration function (3.12).

The black body is connected to a power supplier that heats it up, shown in Figure 3.10 (numbers 1 and 2 respectively). This power supplier heats the black body up by means of several resistances.

The temperature is ranged between room temperature (at about 20 °C) and 90 °C, so that a minimum of 25 points are taken in order to calculate a proper calibration curve. Sequences of images (i.e.: videos) for each desired temperature are recorded in order to obtain a more accurate median of the intensity number of each temperature: over space and over time. Afterwards, these videos are processed by two calibration codes implemented in Matlab.

The first code makes the median of the intensity number of each video over a panel of 20x20 pixels in the center of the image of the black body. In the second code, these intensity levels are matched with the acquired corresponding temperature to numerically obtain the calibration constants of the calibration function. To that end, a calibration function is modeled by Plank's law of radiation because of physical similarities (Astarita and Carlomagno, 2012). Planck's law of radiation evaluates the energy flux (energy rate per body unit surface area) per wavelength emitted by a black body in vacuum. Thus, the function to be used for this purpose in these experiments is:

$$Y_{plank} = \frac{\lambda_1}{e^{(\lambda_2/t)} - \lambda_3} + \lambda_4 \quad (3.1)$$

Once these lambda values are obtained they are used as the calibration constants that correlate the median intensity number of each video with its temperature automatically. This function is then always applied to the data obtained by the camera, providing directly the real temperature of the fluid at

different points of the image. In Figure 3.11 and Figure 3.12 the processing of the images is shown.

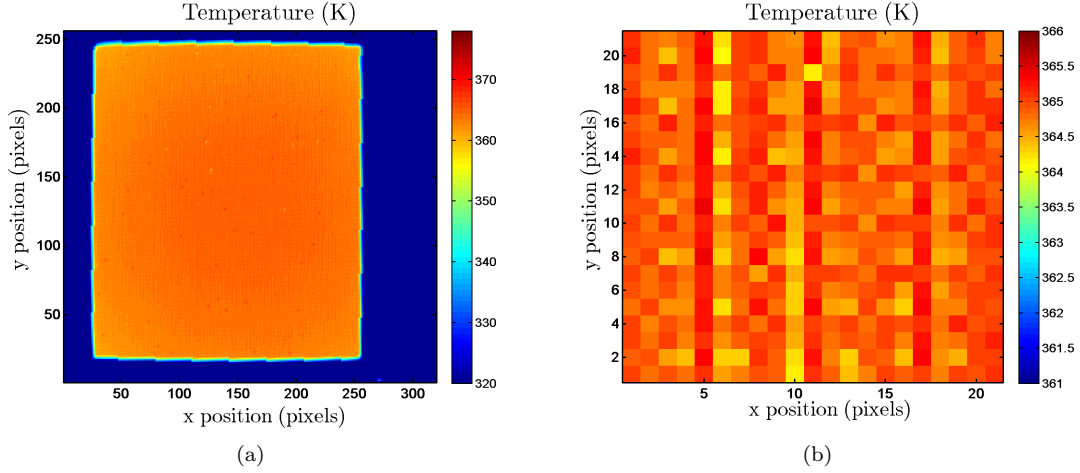


Figure 3.12: Temperature map processing: Temperature map images are treated in the same way as intensity level images were treated previously (Figure 3.11). The translation from intensity levels to temperatures can be directly done on the area of interest (Figure 3.12(b)), where it can be observed that temperature of the 20x20 pixels does not vary more than 0.5 °C, ensuring the proper behavior of the black body.

Several calibrations are needed to determine the proper working conditions of the camera. In first calibrations the camera is placed in front of the black body at 0.5 meter distance, without any other material in between like transparent walls or similar. Both the integration time, i.e.: time the objective is open to take an image or video, and the acquisition frequency of the camera are studied by means of the obtained values of lambda, which make up the fitting curve, and the residual values (difference between each real temperature point and fitting curve).

To begin with, different integration times of the camera are compared: 0.4, 0.5 and 0.6 ms. Figure 3.13 shows their fitting curves (with corresponding lambdas in Table 3.2) and residence values. Better results and fitting of the temperatures and intensity levels were obtained for 0.6 ms compared to 0.4 ms and 0.5 ms, so that integration time does play a role.

A point that does not correspond with the tendency of the rest ones can be seen clearly in Figure 3.13(b). Although not taking this point into account for the calculation of lambda values has been considered, not realistic values were obtained, and therefore it has to be kept in the calculation of the curve. Provided that the chosen integration time is 0.6 ms, no repetition of the calibration at integration time of 0.5 ms was needed.

The behaviour of the camera within different acquisition frequencies is tested next, using 10 Hz and 100 Hz. It can be seen in Figure 3.14 that there is almost no difference between the two cases: both fitting curves and residence values have very similar values and evolutions, therefore it is found that acquisition

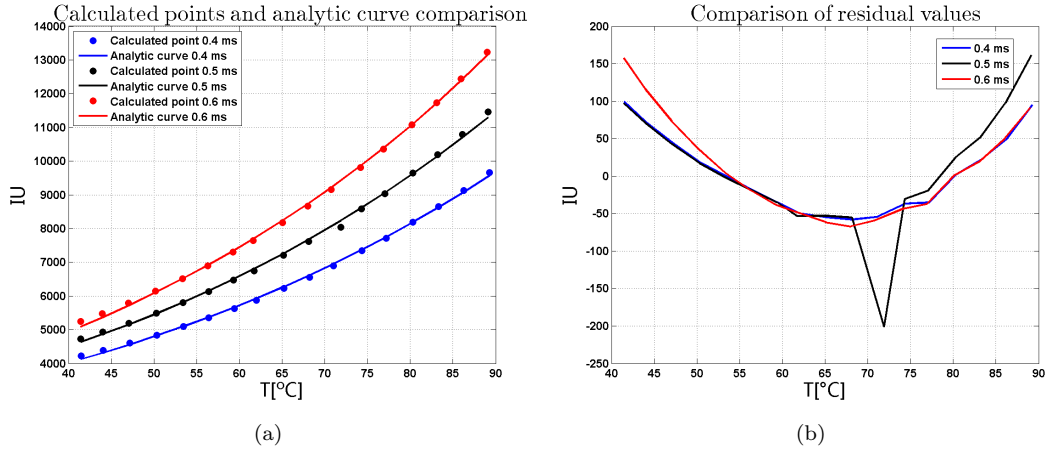


Figure 3.13: The behaviour of the camera with different integration times is shown. In this case, it is highly appreciated that a better curve is obtained for 0.6 ms as integration time.

Integration time (ms)	0.4	0.5	0.6
λ_1	$5.479 \cdot 10^6$	$1.773 \cdot 10^7$	$1.252 \cdot 10^6$
λ_2	$2.382 \cdot 10^3$	$2.715 \cdot 10^3$	$1.775 \cdot 10^3$
λ_3	$5.889 \cdot 10$	$-1.043 \cdot 10$	$3.979 \cdot 10$
λ_4	$1.210 \cdot 10^3$	$1.471 \cdot 10^3$	$-7.515 \cdot 10$
Correlation coefficient	0.969	0.961	0.973
Mean error	-0.065	-0.053	-0.107

Table 3.2: Values of the fitting curve parameters for different integration times

frequency does not play a role in this camera. For better comparison, Table 3.3 shows the constants of each fitting curve.

Acquiring images of the black body at 100 Hz implies that the obtained samples are less spaced in time compared to when acquired at 10 Hz. Knowing that the evolution recorded by the camera both at 10 Hz and 100 Hz is the same, means that no fluctuations are observed by the camera, although they may be present. If fluctuations are present, they are fast enough to not be seen, so no worries are related to them because they do not produce variations. Therefore in this case the phenomenon is considered statistically steady.

Once the proper working conditions of the camera are established, a last calibration is performed before carrying out the experiments. The camera is now placed looking at the black body through the first surface mirror at angles of 45° in order to see how the setup works, i.e., to be aware of how much energy is lost due to the mirror. Table 3.4 and Figure 3.15 show the comparison between previous calibrations and this last one at 10 Hz, where it can be seen similar lambda constants and that the last read intensity values differing slightly over the previous ones (above all as temperature increases). On the same line, the residual values are very similar but slightly smaller than the others.

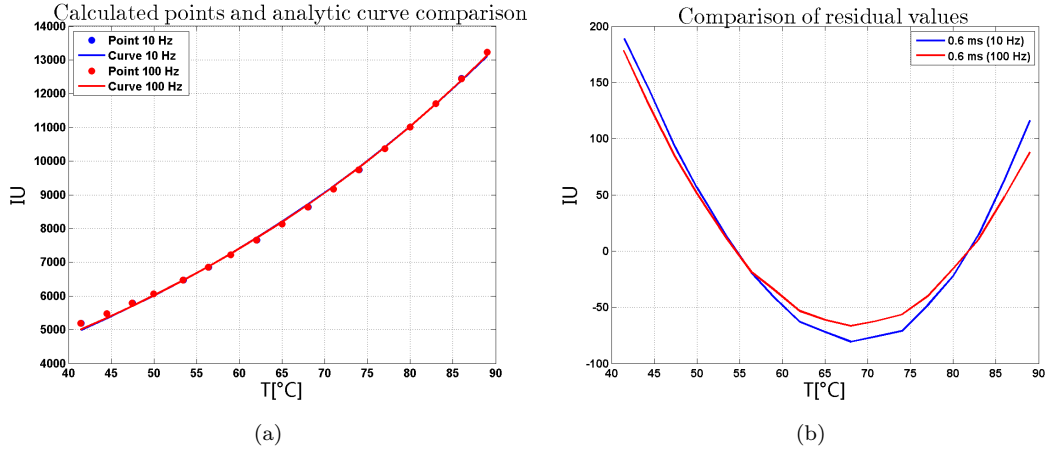


Figure 3.14: Behaviour of the camera with different acquisition frequencies is shown. Although it is not highly appreciated in 3.14(a), it is checked in Table 3.3 which case is the more similar to the reference one.

Acquisition frequency (Hz)	10	100
λ_1	$2.636 \cdot 10^6$	$1.987 \cdot 10^6$
λ_2	$2.001 \cdot 10^3$	$1.919 \cdot 10^3$
λ_3	$4.942 \cdot 10$	$4.898 \cdot 10$
λ_4	-1.366	8.9478
Correlation coefficient	0.966	0.970
Mean error	-0.126	-0.125

Table 3.3: Values of the fitting curve parameters for different acquisition frequencies

Finally the calibration curve used to match correctly data acquired by the camera to real temperatures is shown in Equation 3.2. For the experiments, the camera properties are set such that the integration time is 0.6 ms and the acquisition frequency is 4 Hz.

From this point on, obtained temperature data has been filtered by means of a Gaussian 3D filter (in space and time) in order to reduce noise, and the resolution of the 2D maps is approximately 1 pixel/mm.

$$Y_{plank} = \frac{2.557 \cdot 10^7}{e^{(2.815 \cdot 10^3/t)} - 1.286 \cdot 10} + 1.740; \quad (3.2)$$

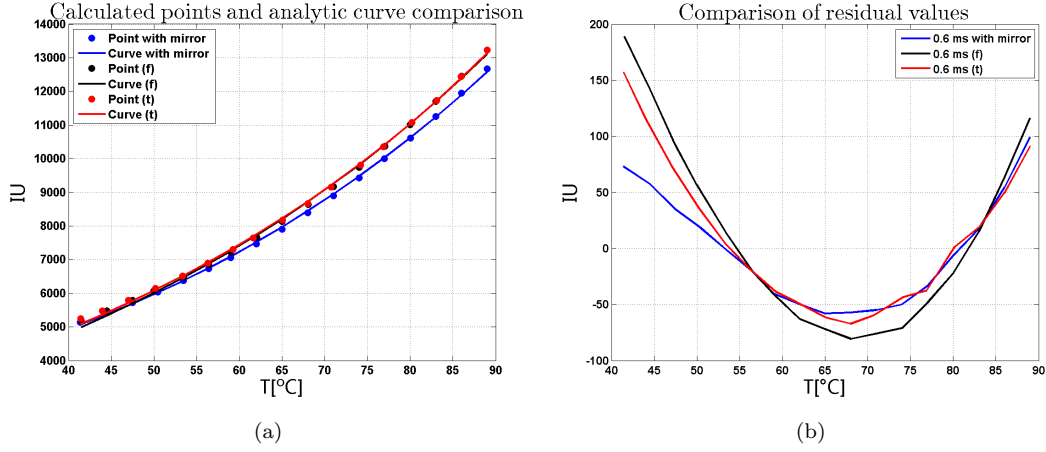


Figure 3.15: The behaviour of the camera under experimental working conditions of the set-up is shown. This case is compared to the previous ones, and it can be seen a slight difference in the behavior of the camera at higher temperatures 3.15(a).

Case	with mirror	acquisition frequency	integration time
λ_1	$2.557 \cdot 10^7$	$2.636 \cdot 10^6$	$1.252 \cdot 10^6$
λ_2	$2.815 \cdot 10^3$	$2.001 \cdot 10^3$	$1.775 \cdot 10^3$
λ_3	$1.286 \cdot 10$	$4.942 \cdot 10$	$3.979 \cdot 10$
λ_4	$1.740 \cdot 10^3$	-1.366	$-7.515 \cdot 10$
Correlation coefficient	0.979	0.966	0.973
Mean error	-0.0125	-0.126	-0.107

Table 3.4: Values of the fitting curve parameters for previous cases are compared to that of the experimental set-up.

Chapter 4

Experimental results

This chapter introduces the obtained results, as well as the processed data that lead to the conclusions presented in next chapter. The modulation of the printed circuit board is made before considering if the unsteady term is important during the transient regime. The transient stages are described afterwards, followed by the origin of some fluid structures and the estimation of the uncertainties of these calculations.

Studied cases The cases studied in the report differ among them in the boundary conditions, that is, applied voltage and intensity (that determine the heat flux input, and thus the initial and overall Rayleigh flux number) and the surrounding conditions such as the ambient temperature. These boundary conditions are shown in Table 4.1 for each case. For all of the cases, Prandtl number Pr is 7, aspect ratio A is 0.5, acquisition frequency is 4 Hz and integration time is 0.6 ms.

Ra_F	Voltage (V)	Intensity (A)	T_{amb} (K)	T_f (K)
$1.3 \cdot 10^{11}$	20	0.76	296.75	295.35
$5.1 \cdot 10^{11}$	40	1.5	296.65	295.45
$1.1 \cdot 10^{12}$	60	2.16	297.25	295.50

Table 4.1: Boundary conditions for each studied case.

4.1 Modulation due to printed circuit board

In order to study the phenomenon explained in previous sections it has to be checked that the infrared camera is able to properly “see” the evolution of the fluid. For that purpose, the response capacity of the circuit printed board to the development of the experiments is analyzed.

Biot number This analysis is based on the study of the thermal evolution of the PCB in the thickness direction. To begin with, it is first proved the Biot number Bi is much lower than unity. The Biot number relates the thermal capacity of the PCB to its conductivity, as Equation 4.1 shows, where in these

experiments h is the calculated convection heat transfer coefficient, s is the characteristic length of the PCB ($s = 0.505 \cdot 10^{-3} m$) and k_s is the through-plane thermal conductivity of the PCB. It has been shown that h is not constant and that k_s is not the same along all directions, however, restrictive values are taken in order to evaluate the critical cases. The meaning of this ratio is that the smaller the value the quicker is the conduction through the thickness, so that a uniform temperature is reached quickly all along the body in question. On the other hand, the greater the value, the longer it takes for the PCB to reach a uniform temperature.

$$Bi = \frac{hs}{k_s} \quad (4.1)$$

The values obtained for Biot number are calculated using the maximum convective heat transfer coefficient h of each case, which depends on each Rayleigh number. Nevertheless, as Table 4.2 shows, Biot number is always much lower than unity, so that T_w at front and back surfaces can be assumed to be the same due to the rapid conduction through the thickness of the board, as it was assumed at the very beginning.

Ra_F	h_{max} ($W/(m^2 K)$)	Bi
$1.3 \cdot 10^{11}$	322.4	0.0420
$5.1 \cdot 10^{11}$	385.2	0.0502
$1.1 \cdot 10^{12}$	392.6	0.0512

Table 4.2: Biot number comparison.

Fourier number Nevertheless, in order to show if the PCB spreads its surface temperature to the rest of the body quick enough to sense the changes of the fluid, a critical time or frequency of the circuit response is needed to be estimated. For that purpose, a basic energy balance in z-direction is done, where spatial and time evolutions of the temperatures of the PCB are compared by means of the heat equation:

$$\frac{\partial T}{\partial t} = \kappa \frac{\partial^2 T}{\partial x^2} \quad (4.2)$$

where $\kappa = k_{PCB} / (\rho_{PCB} c_{PCB})$ is the thermal diffusivity of the printed circuit board. In order to make a better comparison, this equation is non dimensionalized with parameters $T = T_{ref} T^*$, $x = sx^*$ and $t = t_{ref} t^*$, where the asterisk * indicates a non dimensional parameter and s is the thickness of the PCB. In this way the equation ends up being:

$$\frac{\partial^2 T^*}{\partial x^{*2}} = \frac{s^2}{\kappa t_{ref}} \frac{\partial T^*}{\partial t^*} \quad (4.3)$$

where the non dimensionalized term $(\kappa t_{ref}) / (s^2)$ is known as the Fourier number F_0 , that estimates the importance of the spatial and times evolutions of the PCB, as intended from the very beginning. Fourier number can be also expressed as Equation 4.4, meaning that for Fourier numbers greater than 1 the time evolution of the process is more important than the spatial evolution (that

is, the PCB would not be physically able to show the changes the fluid is going through) while for Fourier numbers smaller than unity the spatial evolution is more important (or in other words, the PCB is able to perfectly show the evolution of the fluid since time changes are slower than the capacity of the PCB to show these changes).

$$F_0 = \frac{\frac{\partial T^*}{\partial t^*}}{\frac{\partial^2 T^*}{\partial x^{*2}}} \quad (4.4)$$

Taking into account that no time reference of the temperature change of the PCB can actually be measured within these experiments, a critical time for which spatial and time changes of temperature are equally important is estimated. As it has been shown, in that case the Fourier number has to be equal to unity, giving as a result a critical time $t_{crit} = \frac{s^2}{\kappa}$ or critical frequency $f_{crit} = \frac{\kappa}{s^2}$.

In order for the PCB to be sensitive to the changes of the fluid, the characteristic time of its sensitivity has to be greater than the critical time of the PCB ($t_{cir} > t_{crit}$) or the other way round for the frequencies ($f_{crit} > f_{cir}$). This characteristic time of the PCB is given by the acquisition frequency of the IR camera, since if the variation of the temperatures is faster, the camera is not going to record it, while if it is slower, it will be recorded for sure.

Both the characteristic time of the sensitivity and the critical time of the PCB are the same for all cases, since the acquisition frequency (related to the camera) and the physical properties of the PCB are the same for all. This way, $t_{cir} = 1/4 = 0.25$ s and $t_{crit} = 0.076$ s, fulfilling the previous condition ($t_{cir} > t_{crit}$) and ensuring the PCB is sensitive to the changes of the fluid.

Characteristic time of the phenomenon From this point on, a characteristic time of the fluid evolution is going to be used to non dimensionalize time, and thus being able to compare different cases, not just regarding Rayleigh flux number changes, but also fluid properties or even box changes. In order to do so, a characteristic time is calculated from Equation 4.2, scaling the phenomenon of the fluid as the evolution of the thermal boundary layer thickness δ_t . This way, the characteristic time of the phenomenon is expressed as Equation 4.5 shows. As Mullarney et al. (2004) scaled (Section 1.1), this thermal boundary layer thickness δ_t is of the order of $LRa_F^{-1/6}$, implemented already in Equation 4.5. The characteristic time t_c for each studied case is shown in Table 4.3.

$$t_c \sim \frac{\delta_t^2}{\kappa} \sim \frac{(L_c Ra_F^{-1/6})^2}{\kappa} \quad (4.5)$$

Ra_F	δ_t (m)	t_c (s)
$1.3 \cdot 10^{11}$	$2.1 \cdot 10^{-3}$	124.25
$5.1 \cdot 10^{11}$	$1.7 \cdot 10^{-3}$	78.95
$1.1 \cdot 10^{12}$	$1.5 \cdot 10^{-3}$	60.83

Table 4.3: Characteristic times of the phenomenon for each studied case.

As it can be seen in Table 4.3 the greater the Rayleigh flux number Ra_F the smaller the characteristic time t_c , since as Equation 4.5 shows, they are inversely proportional.

4.2 Unsteadiness evaluation

After checking that the printed circuit board acts actually as a thin foil and that the infrared camera is able to see the heat transfer evolution, it is time to analyze if the unsteady heat transfer term is important or not during transient evolution. In order to do so, the evolutions of the external contributions of the energy balance are compared to the evolution of the internal one.

$$\frac{\rho c s|_{PCB} \frac{\partial T}{\partial t}}{q_j + q_r - q_R - q_k - q_{cv}} \ll 1 \quad (4.6)$$

Starting from the energy balance equation (Equation 2.2) the comparison is made as Equation 4.6 shows, such that the unsteady term can be assumed to be negligible if the sum of all heat fluxes is much greater than the unsteady term.

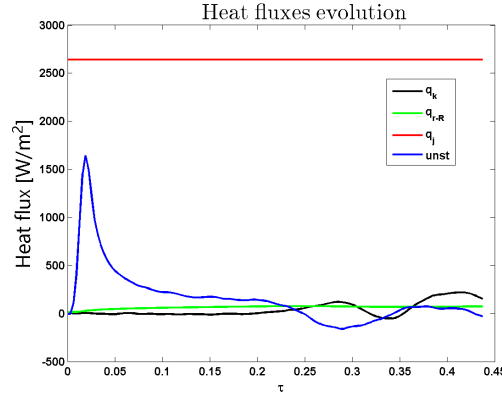


Figure 4.1: Heat fluxes evolution over time. Heat flux due to Joule effect q_j is much higher than the rest of heat fluxes, including the unsteady term. The unsteady term is just important (about the order of magnitude of heat flux due to Joule effect) at the very beginning of the transient process ($\tau = 0.019$). This unsteady term decreases rapidly to be of the order of the rest of heat fluxes ($\tau = 0.07$), so that unsteadiness can be negligible.

As a first approach, orders of magnitude are used for this evaluation. The summation of all heat fluxes acting on the PCB gives an order of magnitude slightly higher to that of the heat flux due to Joule effect, therefore heat flux due to Joule effect is the main external contribution. The time development of each term can be seen in Figure 4.1 where it is appreciated their orders of magnitude to see how much and when each term of the balance energy equation (Equation 2.2) is important.

$$\frac{\rho c s|_{PCB} \frac{\partial T}{\partial t}}{q_j} \ll 1 \quad (4.7)$$

As it was expected, heat flux due to Joule effect is constant over time, while convective and conductive heat fluxes evolve as the wall temperature evolve. The higher order of magnitude of heat flux due to Joule effect with respect to the other terms, make the simplification to Equation 4.7 possible, shown in Figure 4.2. Again, it can be seen that the peak value of the unsteady term is reached at $\tau = 0.019$ but it does not reach the order of the other terms until $\tau = 0.07$.

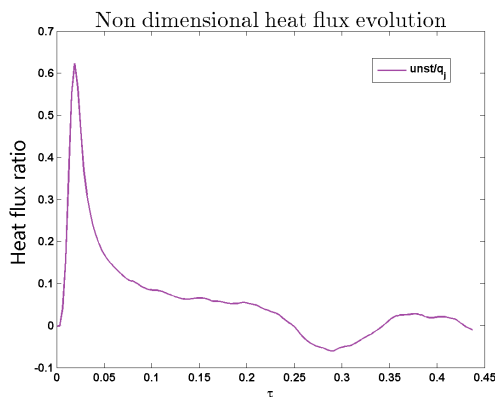


Figure 4.2: Unsteady term compared to heat flux due to Joule effect.

It can be seen that both Figure 4.1 and Figure 4.2 are expressed as a function of the non dimensional time τ . It is of interest how much time the unsteady term is important for each case, so that it is shown in Table 4.4. This table shows the peak time at which the unsteady term is important t_{peak} and the time this unsteady term is of the order of the rest t_r , where the lower the Rayleigh flux number Ra_F the longer in time this term is important. However, as it is shown in Section 4.3, since the transient process evolves until $\tau = 2.4$, this unsteady term stands out just a 3 % of the whole transient regime.

Ra_F	t_{peak} (s)	t_r (s)
$1.3 \cdot 10^{11}$	2.36	8.69
$5.1 \cdot 10^{11}$	1.50	5.53
$1.1 \cdot 10^{12}$	1.16	4.25

Table 4.4: Time importance of unsteady term.

In order to check that recorded images properly show changes in temperatures, some of the parameters are redefined according to Greco et al. (2014) to a critical case: ∂T is the NETD of the camera (shown in Table 3.1) because it is the lowest differential temperature the camera is able to detect and ∂t is

changed to be the inverse of the acquisition frequency because then any other frequency below that one automatically fulfills the condition.

$$\frac{q_j + q_r - q_R - q_k - q_{cv}}{\rho c s|_{PCB} \frac{\partial T}{\partial t}} \approx \frac{q_j}{\rho c s|_{PCB} N E T D f} \gg 1 \quad (4.8)$$

Substituting in Equation 4.8, the approximated ratio gives as a result 63.23, which is much greater than one. Thus, the camera is able to show temperature changes.

4.3 Transient regimes

The main objective of this project is to study the transient evolution of horizontal convection, as mentioned in Section 1. The transient regime ranges from the starting time at which the printed circuit board is switched on and transmits energy to the confined water until water profiles are observed to be repeated over time. Until this point is reached, the transient regime involves three stages, explained hereinafter.

This first explanation of the three different stages is done with the case in which a voltage of 40 V is applied to heat the PCB up, with a current of 1.495 A, ambient temperature of 23.5 ° C and a resulting initial and overall Rayleigh flux number Ra_F is $5.1 \cdot 10^{11}$ (Section 4). It has to be pointed out that these starting conditions work as part of boundary conditions, highly influencing the time development of water circulation inside the box. The evolution of the fluid is presented as 2D maps of Nusselt numbers (explained in Section 2 and Equation 2.1), relating convection and conduction, so that the greater the Nusselt number, the greater convection compared to conduction. This transient evolution is expressed through non dimensional time $\tau = t/t_c$, where t_c was calculated in Section 4.1.

The images are shown as the bottom surface of the printed circuit board seen from below (Figure 2.1), that is, heat exchanger is placed at the left, the right wall is at the right side and there is an horizontal rectangle in the middle of the images that covers a rod that avoids the deflection of the circuit, as mentioned in Section 3.2.

The whole evolution of the transient regime can be watched in this video.

4.3.1 Description of transient regime stages

First stage To begin with, as stated in the experimental procedure (Section 3.1) confined water is at constant ambient temperature before starting the experiments. From the very first moment the printed circuit board is turned on and starts to transmit a constant heat flux F_T to the circuit, so density of water right on top of the PCB decreases as the temperature of the PCB increases due to Joule effect. Locally, the fluid experiences the same boundary conditions as Rayleigh-Bénard convection, in which the fluid is heated from below (by means of the PCB) and cooled from above (due to water above the layer that is instantaneously changing its density). This way, fluid structures similar to Bénard cells are formed, represented as circles in the obtained data because they are seen from the bottom, and get bigger (increase their diameter) as time passes.

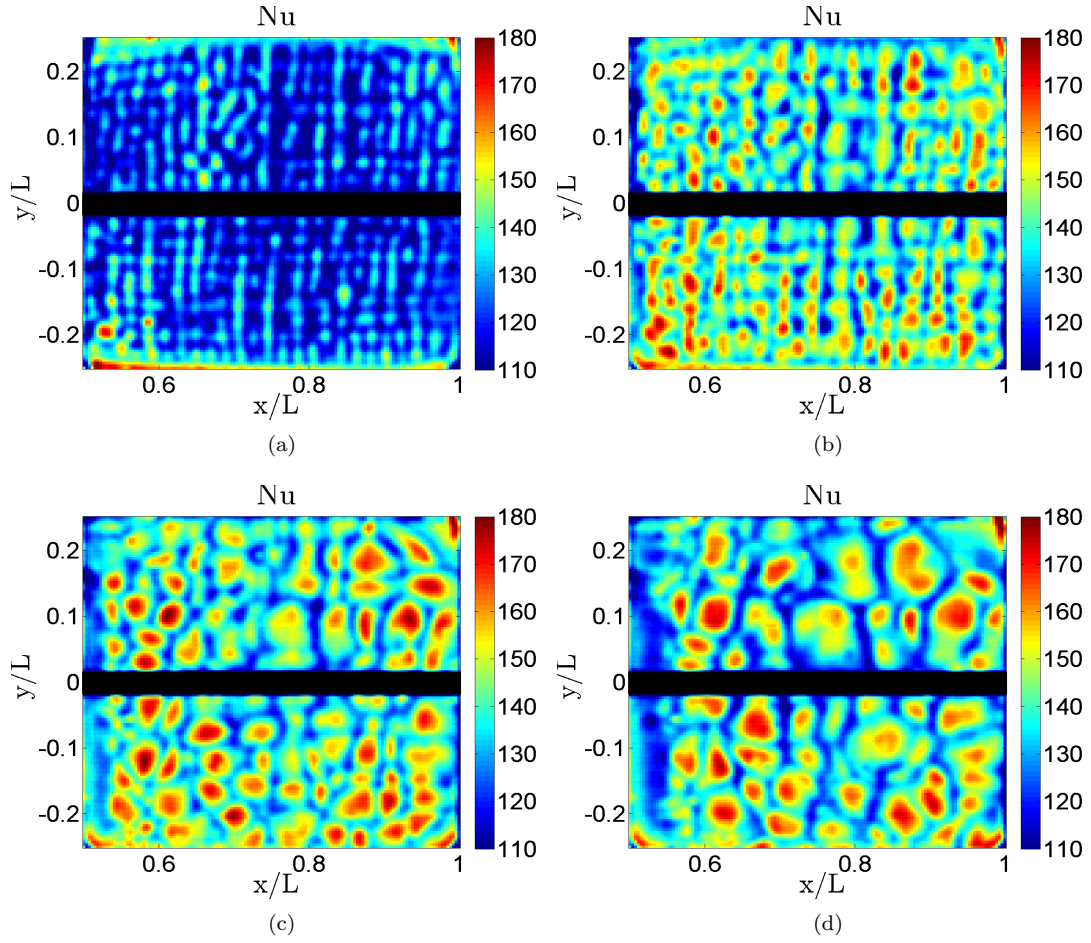


Figure 4.3: Initial structures formation, $Ra_F = 5.1 \cdot 10^{11}$. It is shown that as time passes structures similar to Bénard cells increase their size. 4.3(a) at $\tau = 0.28$, 4.3(b) at $\tau = 0.34$, 4.3(c) at $\tau = 0.41$, 4.3(d) at $\tau = 0.47$.

These structures similar to Bénard cells are formed at the very beginning after the change of temperature of the PCB. These cells get bigger (increase their diameter) as time passes as it can be seen in Figure 4.3(a), Figure 4.3(b) and Figure 4.3(c).

It is noted that greater heat transfer is found in the center of the structures (greater Nusselt number values are seen in Figure 4.3). This first stage extends in time from $\tau = 0$ to $\tau = 0.50$.

Second stage Since fluid is continuously heated from below, and there is no actual cooling boundary condition on the top, tendency of heated fluid is to ascend because its density has decreased. This creates a water circulation in the box: as water right on top of the PCB ascends, water on top of the heat exchanger moves to the top of the PCB so that a counterclockwise circulation is present if looking at the box from outside with the PCB on the right.

Because of the circulation, fluid motion from left to right can be seen in the acquired data (Figure 4.4). This motion moves away the initial structures similar to Bénard cells, resulting in longitudinal instabilities in the form of longitudinal rolls. A great increase of the Nusselt number is observed in this stage, above all in the area where the longitudinal rolls are present, meaning that they greatly improve heat transfer.

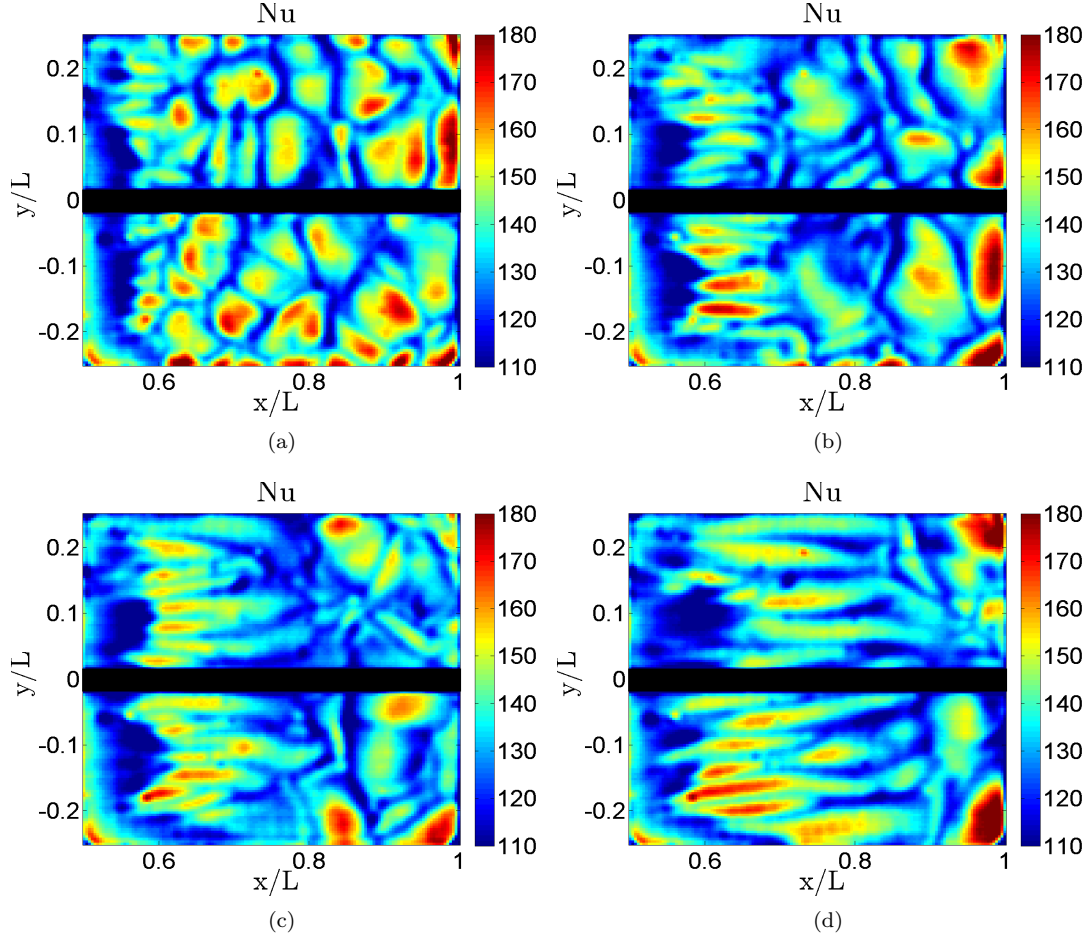


Figure 4.4: Formation of longitudinal rolls, $Ra_F = 5.1 \cdot 10^{11}$. At the same time initial structures are swept away the formation of the longitudinal rolls start, increasing their length as time passes. 4.4(a) at $\tau = 0.56$, 4.4(b) at $\tau = 0.75$, 4.4(c) at $\tau = 0.91$, 4.4(d) at $\tau = 1.10$.

Once the longitudinal rolls have mostly occupied the whole PCB area, they fluctuate for a while before starting the next stage (Figure 4.5). The origin of this rolls is discussed in Section 4.3.2.

This second stage extends in time from $\tau = 0.50$ to $\tau = 1.8$, differentiating the swept of initial cells from $\tau = 0.50$ to $\tau = 1.15$ and the fluctuation of the longitudinal rolls from $\tau = 1.15$ to $\tau = 1.8$.

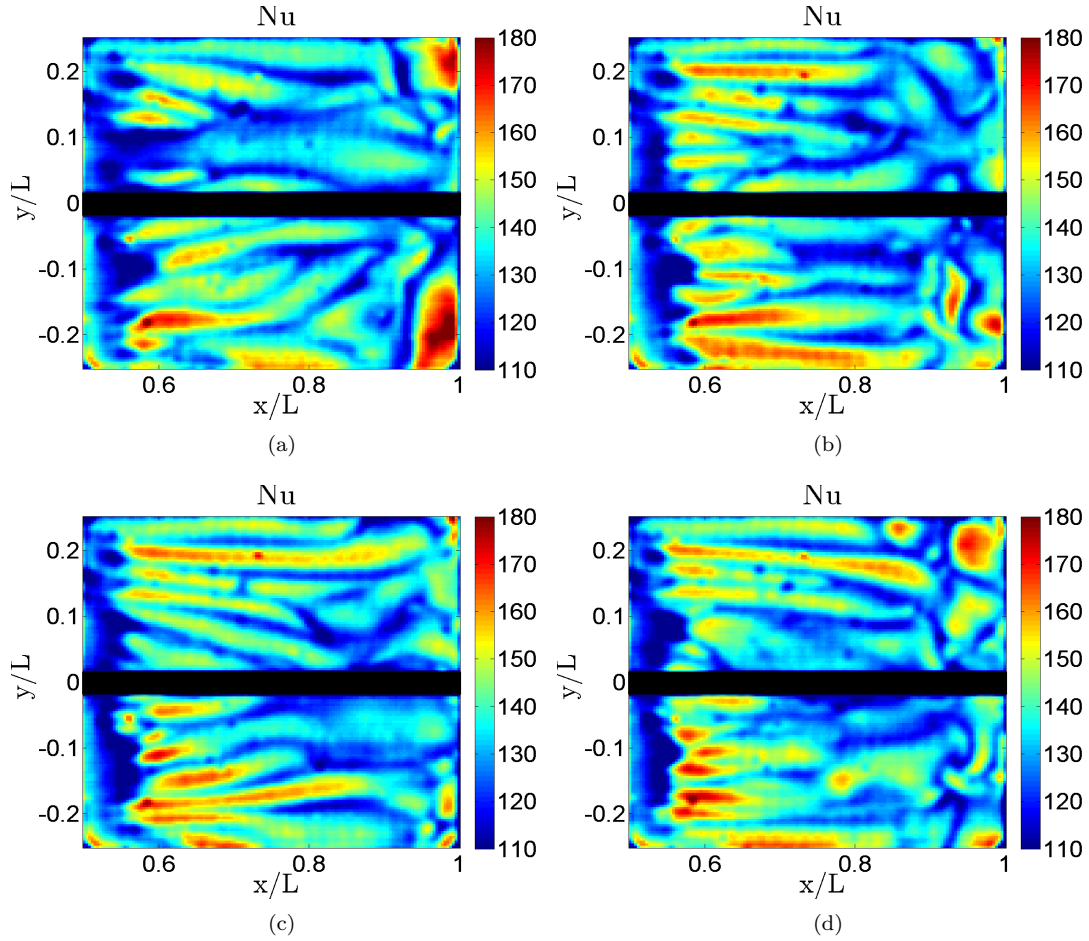


Figure 4.5: Fluctuation of longitudinal rolls, $Ra_F = 5.1 \cdot 10^{11}$. It shows their length is constant and does not increase over time. 4.5(a) at $\tau = 1.23$, 4.5(b) at $\tau = 1.39$, 4.5(c) at $\tau = 1.55$, 4.5(d) at $\tau = 1.70$.

Third stage Before a steady regime is reached, longitudinal rolls become unstable and an important part of these rolls collapse and ascend right next to the right vertical wall of the box as a plume (seen at the right side of the Nusselt number maps). Figure 4.6(a), Figure 4.6(b) and Figure 4.6(c) show the collapse of the longitudinal rolls. It can be observed that compared to previous stages, heat transfer within the whole PCB area is lower in magnitude.

In Figure 4.7 the steady regime is shown. It can be seen that the area occupied by the longitudinal rolls and the plume remains about the same over time, about 1/3 and 2/3 of the PCB respectively. Moreover, heat transfer is still greater in the area where longitudinal rolls are present (greater values of Nusselt number), meanwhile it has decreased where the plume is located.

This third and final transient stage extends in time from $\tau = 1.8$ to $\tau = 2.4$, time at which steady regime is fully reached. A summary of the different non dimensional times at which each stage ends is given in Table 4.5.

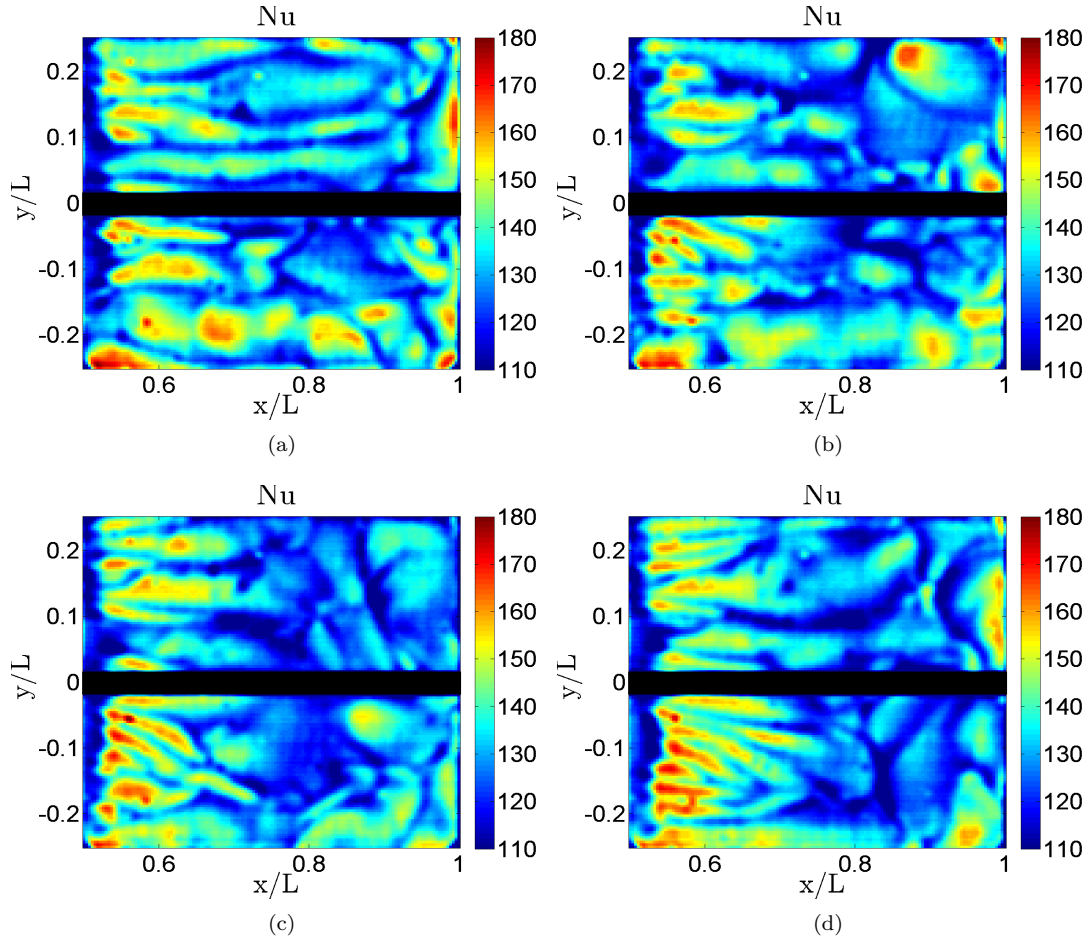


Figure 4.6: Reduction in length of the longitudinal rolls, $Ra_F = 5.1 \cdot 10^{11}$. 4.6(a) at $\tau = 2.02$, 4.6(b) at $\tau = 2.18$, 4.6(c) at $\tau = 2.34$, 4.6(d) at $\tau = 2.5$.

Stage	1 st	2 nd	3 rd
τ	0.5	1.8	2.4

Table 4.5: Non dimensional times at which each stage ends.

4.3.2 Origin of longitudinal rolls

It is going to be checked if the breakdown of the laminar velocity boundary layer, and so the formation of the longitudinal rolls, is not due to a possible curvature of the printed circuit board as according to (Saric, 1994). The formation of this rolls is before hand neglected to be due to viscous or cross-flow phenomena, simply because of the experimental layout and characteristics (no possible cross-flow, water and PCB properties).

The longitudinal rows created due to a curvature of the base are called

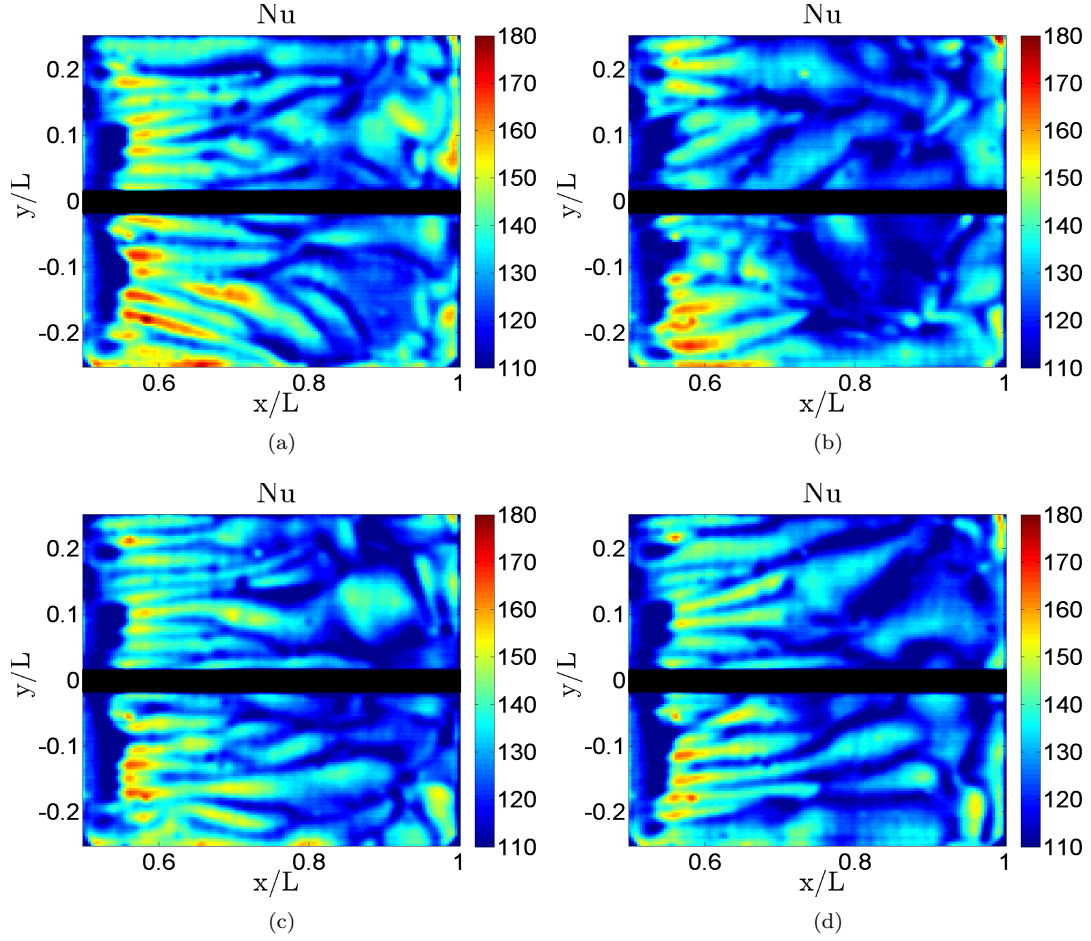


Figure 4.7: Steady regime, $Ra_F = 5.1 \cdot 10^{11}$. It can be seen the longitudinal length of the rolls does not change over time. 4.7(a) at $\tau = 3.76$, 4.7(b) at $\tau = 4.71$, 4.7(c) at $\tau = 6.29$, 4.7(d) at $\tau = 7.56$.

Görtler vortices and are very similar, if they are not, to the ones shown previously in this section. They appear in the boundary layer of concave walls, given in this case by the deflection of the PCB due to the thermal expansion of the copper when it is heated up by Joule effect.

The presence of Görtler vortices is studied by the Görtler number G , which compares centrifugal effects and viscous effects in the boundary layer. Görtler numbers greater than 0.3 prove that presence of the longitudinal rolls is because the velocity boundary layer thickness δ_v is of the order of the radius of curvature R , meaning that a pressure gradient is created along the velocity boundary layer δ_v due to centrifugal forces.

Since no method is available to experimentally measure the velocity boundary layer thickness δ_v , the use of Görtler number is needed. Görtler number G is defined in Equation 4.9, where ζ is the wall curvature ($\zeta = \frac{\eta L_c}{R}$), η is the viscous parameter and L_c and R are the reference length and the radius of curvature of

the PCB.

$$G = \sqrt{\frac{\zeta}{\eta}} = \sqrt{\frac{L_c}{R}} \quad (4.9)$$

It is seen that Görtler number is easily reduced to a fraction where the only value left to be calculated is the radius of curvature R . To do so in a conservative way, a PCB deflection of $d = 1mm$ is estimated. Taking into account the rest of lengths of the PCB the calculation of the radius of curvature is straightforward thanks to Pitagoras' theorem (Figure 4.8, Equation 4.10).

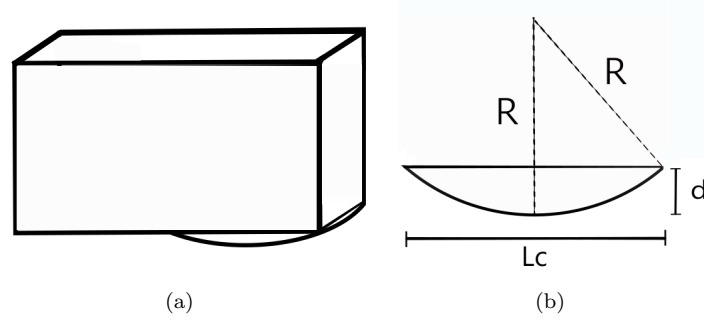


Figure 4.8: Radius of curvature of the printed circuit board. 4.8(a) Exaggerated deflection of the printed circuit board. 4.8(b) Calculation of the radius deflection, also shown in Equation 4.10.

$$R = \sqrt{\left(\frac{L_c}{2}\right)^2 + (R - d)^2} \quad (4.10)$$

In the end, a radius R of approximately 2.81 m is obtained, resulting in a Görtler number G of 0.231; therefore, the velocity boundary layer thickness δ_v is not of the order of R and thus pressure across itself is constant. The results confirms that the origin of the longitudinal rolls is not due to the deflection of the printed circuit board.

4.4 Rayleigh number study

The behavior of the fluid under different Rayleigh numbers is going to be studied. For that purpose, the evolution in time of the three different stages shown in Section 4.3 is observed. However, at a first approach it is of common sense that the greater the voltage used, the greater the difference of temperature created by the PCB, causing this transient regime to be faster.

The study is performed for three different boundary conditions (Table 4.1):

1. Rayleigh flux number of $Ra_F = 1.3 \cdot 10^{11}$
2. Rayleigh flux number of $Ra_F = 5.1 \cdot 10^{11}$
3. Rayleigh flux number of $Ra_F = 1.1 \cdot 10^{12}$

The comparison is done in terms of both dimensional and non dimensional time (t and τ) for each case. This way, the evolution of the fluid in the first and third cases are compared to the reference one. It is noted that different Nusselt number scales are used for each case.

First stage To begin with, the first stage is compared in Figure 4.9, where comparison is done at $\tau = 0.41$. As it can be compared to Figure 4.3(c), the greater the voltage applied to the printed circuit board, the faster the increase in magnitude of the initial cells (t decreases as the Rayleigh flux number increases for the same τ). In other words, structures similar to Bénard cells get bigger sooner as Rayleigh flux number increases.

Moreover, the higher the applied voltage or the Rayleigh flux number Ra_F the higher the obtained Nusselt numbers, so the stronger the heat transfer.

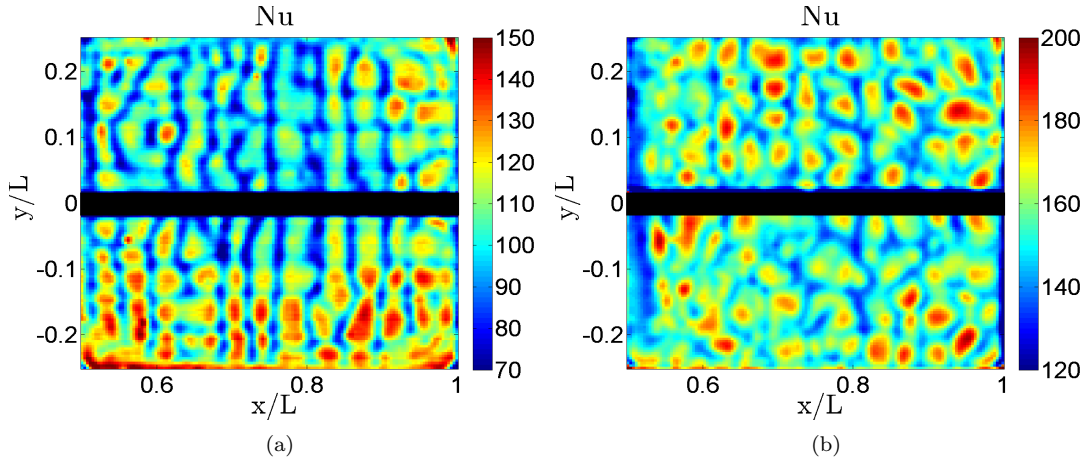


Figure 4.9: Initial structures comparison at same evolution time $\tau = 0.41$ for different Rayleigh flux numbers Ra_F . Initial structures are developed much faster for $Ra_F = 1.1 \cdot 10^{12}$ ($t = 25s$, 4.9(b)) than for $Ra_F = 5.1 \cdot 10^{11}$ ($t = 32s$, 4.3(c)) or $Ra_F = 1.3 \cdot 10^{11}$ ($t = 50s$, 4.9(a)).

In Table 4.6 the duration of this first transient stage in which initial cells are formed is shown (t_d). As it was said before, the higher the voltage the faster the evolution within the stages, so at 60 V the duration of this first stage is smaller than for the other cases. t_0 refers to the initial time of the stage while t_f is the final time.

Ra_F	t_0	t_f	t_d
$1.3 \cdot 10^{11}$	0 s	58 s	58 s
$5.1 \cdot 10^{11}$	0 s	37 s	37 s
$1.1 \cdot 10^{12}$	0 s	29 s	29 s

Table 4.6: First transient stage duration for each case.

Second stage The creation of the longitudinal rolls stage is compared at $\tau = 0.91$. As it was mentioned before, the greater the voltage applied or the greater the Rayleigh flux number, the sooner the development, as it can be seen in Figure 4.10. The same can be seen for time development $\tau = 1.55$, non dimensional time at which the longitudinal rolls are fluctuating (Figure 4.11).

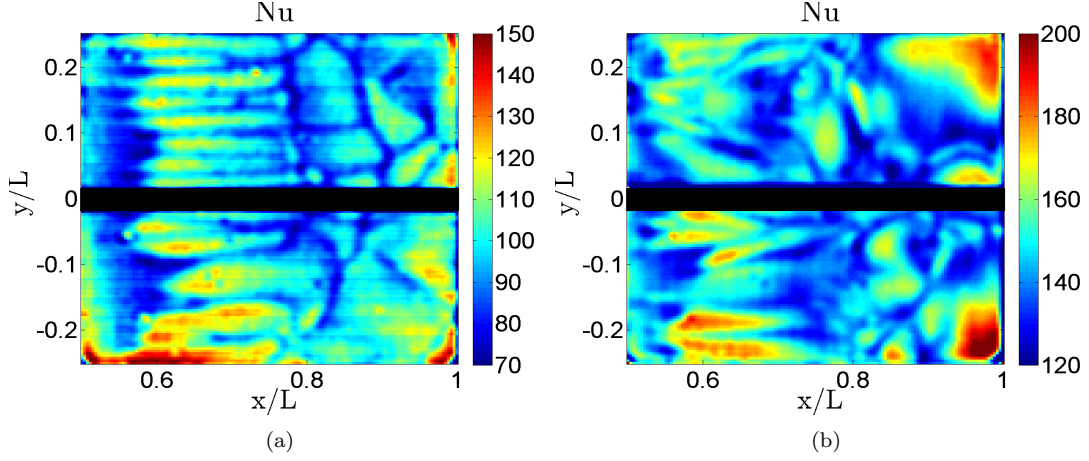


Figure 4.10: Longitudinal rolls development comparison at same evolution time $\tau = 0.91$ for different Rayleigh flux numbers Ra_F . Again, the development is much faster for $Ra_F = 1.1 \cdot 10^{12}$ ($t = 55s$, 4.10(b)) than for $Ra_F = 5.1 \cdot 10^{11}$ ($t = 1min12s$, 4.4(d)) or $Ra_F = 1.3 \cdot 10^{11}$ ($t = 1min53s$, 4.10(a)).

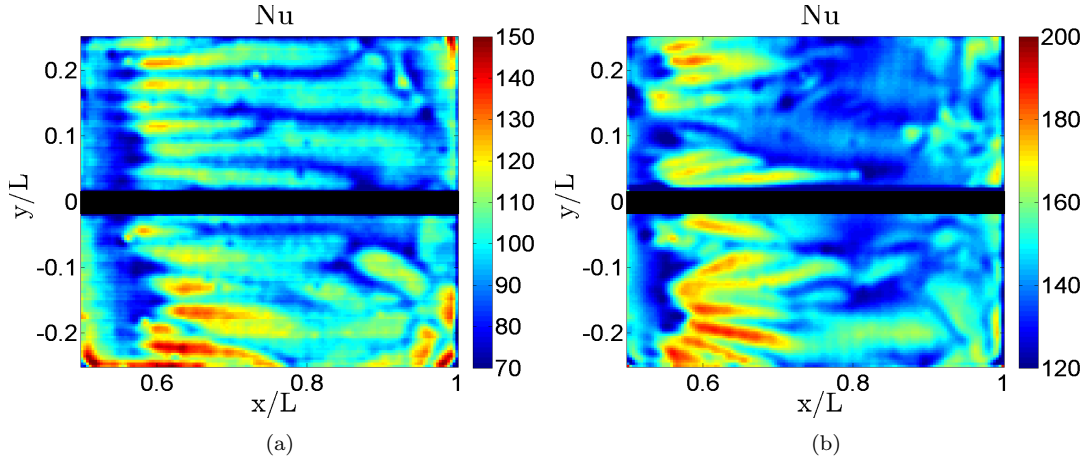


Figure 4.11: Longitudinal rolls fluctuation at the same evolution time $\tau = 1.55$ for different Rayleigh flux numbers Ra_F . This stage is reached later in time for $Ra_F = 1.3 \cdot 10^{11}$ ($t = 3min12s$, 4.11(a)) compared to $Ra_F = 5.1 \cdot 10^{11}$ ($t = 2min2s$, 4.5(d)) or $Ra_F = 1.1 \cdot 10^{12}$ ($t = 1min34s$, 4.11(b)).

As it can be seen in Figure 4.10 and Figure 4.11, longitudinal rolls are more unstable as Ra_F increase. This means that buoyancy forces are greater and

thus water tend to ascend closer to the heat exchanger, instead of just on the right side, next to the vertical wall.

In Table 4.7 the duration of the second transient stage for each case is shown (t_d). It is differentiated among the starting time of the stage (t_0), the starting time at which longitudinal rolls fluctuate and has initial structures has been swept (t_1) and the final time longitudinal rolls fluctuate and start decreasing in length.

Ra_F	t_0	t_1	t_f	t_d
$1.3 \cdot 10^{11}$	58 s	2 min 17 s	3 min 43 s	2 min 45 s
$5.1 \cdot 10^{11}$	37 s	1 min 27 s	2 min 22 s	1 min 45 s
$1.1 \cdot 10^{12}$	29 s	1 min 7 s	1 min 49 s	1 min 21 s

Table 4.7: Second transient stage duration for each case.

Third stage The longitudinal rolls collapse is given at about $\tau = 2.02$ and steady regime can be clearly seen already reached at about $\tau = 6.3$. These comparisons are shown in Figure 4.12 and Figure 4.13 respectively.

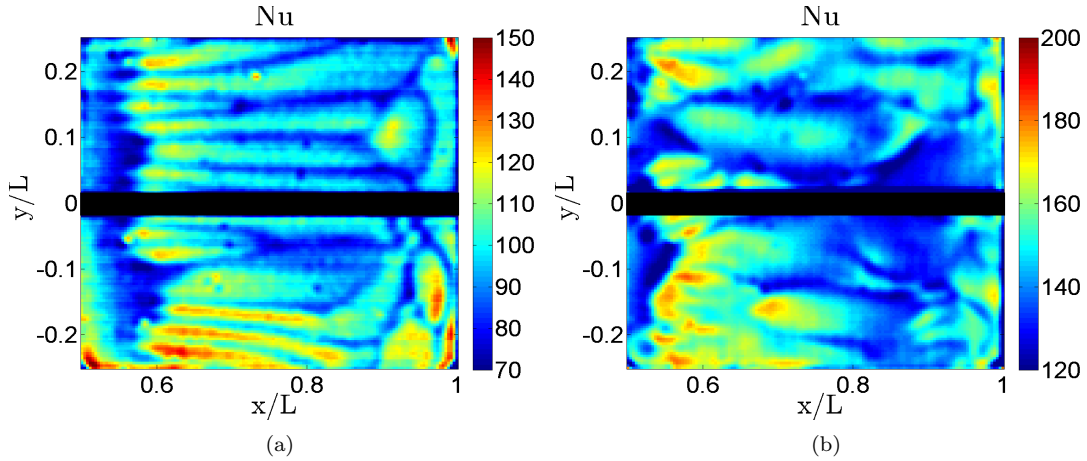


Figure 4.12: Longitudinal rolls decrease at the same evolution time $\tau = 2.02$ for different Rayleigh flux numbers Ra_F . This reduction in length is reached later in time for $Ra_F = 1.3 \cdot 10^{11}$ ($t = 4min11s$, 4.12(a)) compared to $Ra_F = 5.1 \cdot 10^{11}$ ($t = 3min40s$, 4.6(a)) or $Ra_F = 1.1 \cdot 10^{12}$ ($t = 2min3s$, 4.12(b)) .

As mentioned in previous section, heat transfer decreases in magnitude once the longitudinal rolls start to collapse. Moreover, as stated in previous section, for higher Rayleigh flux number Ra_F the ascending plume start to develop nearer to the heat exchanger side.

In Table 4.8 the duration of the third transient stage t_d is shown for each case. It is differentiated among the starting time of the stage (t_0), at which the longitudinal rolls decrease, and the final time (t_f) where the steady regime is reached and the longitudinal rolls do not vary its shape.

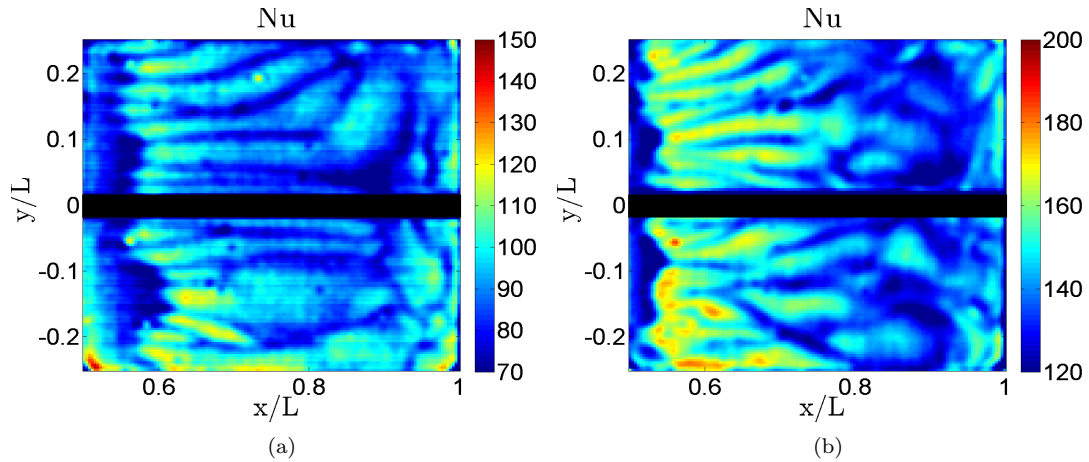


Figure 4.13: Established steady regime at the same evolution time $\tau = 6.3$ for different Rayleigh flux numbers Ra_F . This stage can be seen fully reached at $t = 13\text{min}2\text{s}$ for $Ra_F = 1.3 \cdot 10^{11}$ (4.13(a)), at $t = 8\text{min}17\text{s}$ for $Ra_F = 5.1 \cdot 10^{11}$ (4.7(d)) and at $t = 6\text{min}23\text{s}$ for $Ra_F = 1.1 \cdot 10^{12}$ (4.13(b)).

Ra_F	t_0	t_f	t_d
$1.3 \cdot 10^{11}$	3 min 43 s	4 min 50 s	1 min 7 s
$5.1 \cdot 10^{11}$	2 min 22 s	3 min 5 s	42 s
$1.1 \cdot 10^{12}$	1 min 49 s	2 min 22 s	33 s

Table 4.8: Third transient stage duration for each case.

4.5 Evaluation of measured data

In order to qualify the reliability of the results quantitative errors of the measurements are calculated. These quantitative indicators are used for better comparison among different results or with reference values. For this purpose, BIPM et al. (1995) is used because it offers a readily implemented, easily understood, and generally accepted procedure for characterizing the uncertainty of a measurement result.

To begin this characterization the measurand, the method of measurement, and the measurement procedure have to be specified. A result of a measurement is only estimation so that a result is complete when accompanied by an uncertainty of that estimate. This uncertainty is usually referred to as an error, in which two components may be distinguished: random component and systematic component.

Random error is that unpredictable or related to temporal or spatial variations, whose effects are repeated in repeated measurements and cannot be mitigated for a single test. However, random error can be reduced by making more observations.

On the other hand, systematic error can be reduced if it arises from a recognized effect such as assumptions, approximations, finite instrument resolution or apparently similar working conditions. If this effect can be quantified, a

correction factor can be applied to reduce the systematic error.

The uncertainty of a result is evaluated using a mathematical model of the measurement and the law of propagation of uncertainty. For a well-characterized measurement under statistical control there are errors already quantified, as it is the case of universal constants, material properties or measurements taken with specified instruments.

However, for those cases in which a constant is evaluated with the use of an instrument, usually a sample of n independent observations is taken in order to calculate the variance of the arithmetic mean. This is the case of for example T_w , for which the calibration images are used to obtain the standard deviation of the pixels.

On the other hand, in most cases, a measurand Y is not measured directly, but is determined from x_N other quantities, as it is the case of Nusselt number Nu and heat transfer coefficient h , in which their values depend on other calculated parameters. For these cases, the uncertainty is calculated as Equation 4.11 shows.

$$unc(Y) = \sqrt{\sum_{x_i}^N \left(\frac{\partial Y}{\partial x_i}\right)^2 (unc_{x_i})^2} \quad (4.11)$$

Following this last equation two spatially separated points of the PCB images are taken to calculate the uncertainties of the experiments. As it can be seen all the uncertainties for the convective heat transfer coefficient h lay in the range $1 - 2 W/(m^2K)$, which is a very acceptable value given that this coefficient is usually of the order of $200 - 300 W/(m^2K)$, therefore uncertainties are of the order of $1 - 2 \%$ (shown in Table 4.9). For Nusselt number Nu the uncertainty is of the order of 1% , as it can be seen in Table 4.10.

Ra_F	h_1	$unc(h_1)$	h_2	$unc(h_2)$
$1.3 \cdot 10^{11}$	179.11	1.09	186.24	1.15
$5.1 \cdot 10^{11}$	296.42	2.2	237.59	1.7
$1.1 \cdot 10^{12}$	294.51	2.06	283.02	1.97

Table 4.9: Uncertainty values of h for different Rayleigh flux numbers. The same two points have been considered for all the calculations in order to be consistent with the possible fluctuations of the measurements. Moreover, conservative values have been used where possible to obtain realistic uncertainties. The heat transfer coefficient and its uncertainties in $W/(m^2K)$.

Ra_F	Nu_1	$unc(Nu_1)$	Nu_2	$unc(Nu_2)$
$1.3 \cdot 10^{11}$	89.56	0.67	93.12	0.70
$5.1 \cdot 10^{11}$	148.21	1.7	118.79	1.3
$1.1 \cdot 10^{12}$	147.26	1.62	141.512	1.55

Table 4.10: Uncertainty values of Nu for different Rayleigh flux numbers. The same two points have been considered for all the calculations in order to be consistent with the possible fluctuations of the measurements. Moreover, conservative values have been used where possible to obtain realistic uncertainties.

In Table 4.11 the uncertainty of each component that is used to calculate the uncertainty of the convective heat transfer coefficient h and Nusselt number Nu is shown.

Parameter	Units	Uncertainty (%)	Uncertainty information
ϵ		0.5	50 % of the minimum reading
ρ_{PCB}	kg/m^3	0.1	50 % of the minimum reading
σ	$W/(m^2K^4)$	$2.1 \cdot 10^{11}$	Uncertainty of a universal constant
I	A	0.2	Standard deviation given by the manufacturer
k_{PCB}	$W/(mK)$	0.01	50 % of the minimum reading
k_f	$W/(mK)$	0.5	50 % of the minimum reading
L	m	0.05	50 % of the minimum reading
L_c	m	0.05	50 % of the minimum reading
s	m	0.0001	50 % of the minimum reading
t	s	0.5	50 % of the minimum reading
T_w	K	1.8	Standard deviation given by the manufacturer
T_{amb}	K	1.8	Standard deviation given by the manufacturer
T_f	K	1.8	Standard deviation given by the manufacturer
V	V	0.03	Standard deviation given by the manufacturer

Table 4.11: Uncertainty values of parameters. Every shown value is used for the calculation of both the uncertainty of the convective heat transfer coefficient h and the Nusselt number Nu , except the longitude of the box L where heat transfer takes place and the thermal coefficient of water k_f that are just used for the uncertainty of the Nusselt number Nu .

Chapter 5

Conclusions

In this final section of the project the main conclusions are going to be presented. These conclusions include experimental results, possible improvements of the experimental setup and future work to be done regarding the obtained results.

Experimental results After the assembly of the experimental set up, the experiments were carried out once the proper working conditions of the infrared camera were defined (independent on the acquisition frequency and integration time of 0.6 ms) and once it was verified that the printed circuit board actually acts as a heated thin foil ($Bi \ll 1$), being able to "see" the evolution of the fluid properly ($t_{cir} = 0.25 > t_{crit} = 0.076$). The unsteady term of the fluid evolution was checked to be negligible, simplifying the calculation of the heated thin foil method.

First, the transient regime study of horizontal convection is commented. This study has shown that three main stages are differentiated in this regime:

1. Formation of Rayleigh-Bénard cells: The printed circuit board is turned on and transmits constant heat flux F_T to the circuit, so density of water right on top of the PCB decreases as temperature of the PCB increases due to Joule effect. Locally, the fluid experiences similar boundary conditions as Rayleigh-Bénard convection so that structures similar to Bénard cells are formed and get bigger (increase their diameter) as time passes. Heat transfer is greater in the center of Rayleigh-Bénard cells. This first stage extends in time from $\tau = 0$ to $\tau = 0.50$.
2. Formation of longitudinal rolls: Since fluid is continuously heated from below tendency of heated fluid is to ascend because its density has decreased. This creates a water circulation in the box: as water right on top of the PCB ascends, water on top of the heat exchanger moves to the top of the PCB so that a counterclockwise circulation is formed if looking at the box from outside with the PCB on the right.

Because of circulation, fluid motion from left to right can be seen in acquired images. This motion moves away the initial cells, resulting in longitudinal instabilities in the form of longitudinal rolls. A great increase of the Nusselt number is observe in this stage, above all in the area where the longitudinal rolls are present, meaning that they greatly improve heat

transfer. The swept of structures similar to Rayleigh-Bénard cells goes from $\tau = 0.50$ to $\tau = 1.15$.

Once the longitudinal rolls have mostly occupied the whole PCB area, they fluctuate for a while before starting the next stage. The origin of this rolls was proved to be due to instabilities and not because of possible deflection of the PCB when it is heated up. The fluctuation of the longitudinal rolls from $\tau = 1.15$ to $\tau = 1.8$.

3. Before a steady regime is reached, the longitudinal rolls decrease in length progressively and an important part of water on top of the PCB would be seen ascending right next to the right vertical wall as a plume. Lower values of Nusselt number are obtained where the plume is present, therefore heat transfer is lower in that area. This third and final transient stage extends in time from $\tau = 1.8$ to $\tau = 2.4$.

In the steady regime, two main areas are distinguished: longitudinal rolls and a plume that occupy 1/3 and 2/3 of the PCB area respectively. The first ones transfer heat greatly (greater values of Nusselt number) compared to the second one, that has lower Nusselt number values.

According to the Rayleigh number study, the greater this ratio the faster the evolution of the transient regime within its three stages. The characteristic time t_c of each case made possible the easy comparison between them through the non dimensional time τ .

Higher Nusselt numbers are found for the higher Rayleigh number case, meaning that the higher the voltage applied the greater the convective heat transfer within the fluid, making a faster development of the transient regime.

Moreover, in the second stage of the transient regime, longitudinal rolls are more unstable as Ra_F increase. This means that buoyancy forces are greater, and therefore water tend to ascend closer to the heat exchanger, instead of just on the right side, next to the vertical wall.

Uncertainties of the convective heat transfer coefficient h and Nusselt number Nu were shown to be about 2% and 1% respectively.

Possible improvements Based on present experience it can be ensured that some repairs can be done to improve the experimental set-up. Although the box that confines the fluid was assembled not so long ago, it is of interest if:

- The joint between the printed circuit board and the heat exchanger is ensured, as well as the joints among walls, bottom and top covers, so that no water losses occur.
- A vacuum system of determined characteristics is implemented to the top of the box, so that an aspect ratio study can be performed. The water would not fill the entire box but there would not be air inside, avoiding changes in water properties where contact between air and water is present.
- The walls of the box are properly polished to be able to perform PIV (Particle Image Velocimetry) studies in the future, for example.

Future development Similar to the improvements suggested of the box, experimental procedures and post-experimental processes can be enhanced too:

- Although restrictive values have been used throughout the whole evaluation of the project, it is of interest to use real experimental data. For example, an exact critical time t_{crit} could be estimated processing the data with a temporal filter that shows the real critical frequency of the fluid structures f_{crit} , instead of being given by the assumption of time variations equally important to spatial variations (or Fourier number F_0 equal to 1).
- The use of a more powerful infrared camera would provide a better resolution of the acquired images.
- The project has been focused on the temperature measurement of the fluid evolution in that area of the box where greater and important changes were expected. However, deeper conclusions and results can be addressed with a whole view of the process. This can be done by means of Particle Image Velocimetry (PIV), a flow visualization method. Using this optical procedure the instantaneous velocity field of the fluid can be observed, and thus obtain other points of view of the experiment, such as from side walls, or further information about heat transfer in the longitudinal rolls, for example.
- Further research include study of different combination of the parameters that drive horizontal convection: Prandtl number Pr , Rayleigh number Ra and aspect ratio A of the box.

Appendix A

Codes

Hereinafter, some of the codes used in the project are shown. The first one shows the calculation of the temperature of the fluid T_{cold} (Code A.1). Variables depending on each studied case are saved in different .mat files. After that, the heated thin foil code calculates the convective heat transfer coefficient h and the Nusselt number Nu (Code A.2), followed by the code used to create figures with a specific format and the one that creates a video out of the displayed images (Code A.4 and Code A.3). Small clarifications are made throughout the codes.

It has to be noted that the function ReadRT is in charge of convert the data acquired by the camera (.inc, .pod, .sbp, .scg, .sco and .sfmov files) to 2D maps of intensity numbers or temperatures. However, it cannot be displayed in this project due to copyright license.

```
1 %%%%%%%%%%%%%%%%%%%%%%%%%%%%%%%%%%%%%%%%%%%%%%%%%%%%%%%%%%%%%%%%%%%%%%%%%%  
2 %  
3 %                                COLD TEMPERATURE CODE                                %  
4 %  
5 %%%%%%%%%%%%%%%%%%%%%%%%%%%%%%%%%%%%%%%%%%%%%%%%%%%%%%%%%%%%%%%%%%%%%%%%%%  
7 addpath('C:\horizontal_convection\Tcold');  
8 path='C:\horizontal_convection\Tcold'; %folder where data is stored  
9 type='*.inc'; % type of file to be processed  
10 names=getfiles(path,type); % get name of different files  
11 [names,index]=sort_nat(names); % order names alphabetically  
13 for i=1:numel(names)  
14     [pathstr filenames extension]=fileparts(names{i,1});  
15     [Gl numfr]=ReadRT(filenames,1);  
16     for j=1:numfr  
17         [Gl numfr]=ReadRT(y,j);  
18         meanMatimage(j) = mean2(Gl.Mat(47:220,56:211));  
19         meanTimage(j) = mean2(Gl.T(47:220,56:211)) -273.15; % [*C]  
20     end  
21     meanMatseq(i) = mean2(meanMatimage);  
22     meanTseq(i) = mean2(meanTimage); % [*C]  
23 end  
25 Tcold = meanTseq; % [*C]  
27 save('Tcold','Tcold')
```

Code A.1: Cold temperature code. T_{cold} is what is called in the process T_f , that

is, initial temperature of the fluid. This code is part of the processing codes used to relate intensity levels and temperatures in calibrations.

```

%%%%%%%%%%%%%%%%%%%%%%%%%%%%%%%%%%%%%%%%%%%%%%%%%%%%%%%%%%%%%%%%%%%%%%%%%%%%%%
2  %                                     %
%                                     HEATED THIN FOIL CODE                                     %
4  %                                     %
%%%%%%%%%%%%%%%%%%%%%%%%%%%%%%%%%%%%%%%%%%%%%%%%%%%%%%%%%%%%%%%%%%%%%%%%%%%%%%

6
close all
8 clear all
clc

10
addpath('C:\horizontal_convection');
12 path='C:\horizontal_convection'; %folder where images are stored
type='*.inc'; %type of file
14 names=getfiles(path,type);
[names,index]=sort_nat(names); %acquire name of data

16
%loading processed variables and data
18 load('Tcold','Tcold'); % Const cold temp acquired by camera
Tcold=Tcold+273.15; % [K]
20 load('Data','Tamb','Intensity','Volt')
load('Image','xR','xL','yD','yU') % Pixels that limits the area
of interest of the images

22
%%% Printed circuit board data
24 sc=5e-6; % [m] thickness copper
wc=1.8e-3; % [m] width copper
26 lambdac=401; % [W/(mK)] conductive coeff copper [in-plane]
kc=401; % [W/(mK)] conductive coeff copper [through-plane]
28 cpc=0.39e3; % [J/(kgK)] specific heat capacity copper
rhoc=8.96e3; % [kg/m^3] density copper

30
sf=0.5e-3; % [m] thickness FR-4
32 wf=2e-3; % [m] width FR-4
lambdaf=1.04; % [W/(mK)] conductive coefficient FR-4 [in-plane]
34 kf=0.3; % [W/(mK)] conductive coefficient FR-4 [throughplane]
cpf=0.6e3; % [J/(kgK)] specific heat capacity FR-4
36 rhof=1.85e3; % [kg/m^3] density FR-4

38 wcf=wc/wf;

40 kboardY = wcf*sc*lambdac+sf*lambdaf; % [W/(K)] [in-plane]
kboardX = ((1-wcf)/(sf*lambdaf)+(wcf)/(sf*lambdaf+sc*lambdac))^( -1);
% [W/(K)] [in-plane]
42 kboard = kc*(sc*wc)/(sc*wc+sf*wf)+kf*(sf*wf)/(sc*wc+sf*wf);
% [W/(mK)] [through-plane]
cp=cpc*(sc*wc)/(sc*wc+sf*wf)+cpf*(sf*wf)/(sc*wc+sf*wf);
% [J/(kgK)] specific heat capacity PCB
44 m=rhoc*sc*75*wc*0.15+rhof*sf*0.15^2; % [kg] mass PCB
g=9.80665; % [m/s^2] gravity constant

46
tboard = 505e-6; % [m] thickness PCB
48 Aboard = 0.15^2; % [m^2] area PCB
rho=m/(Aboard*sf); % [kg/m^3] density PCB
50 Lcheat= 0.3; % [m] characteristic lenght where heat transfer
occurs (PCB and heat exchanger)
Lcboard = 0.15; % [m] characteristic lenght of the PCB
52 sigma = 5.67E-8; % [W/(m^2 K^4)] Stefan-Boltzmann constant
epsilonboard = 0.95; % [] epsilon coefficient PCB

54

```

```

Qj=Intensity*Volt/Aboard; %[W/m^2] Heat flux per unit area due to
    Joule effect
56
%% Water data
58 kwater = 0.6;          %[W/(mK)] water thermal conductivity
    alphawater = 0.000207; %[1/K] water thermal expansion coefficient
60 nuwater = 1.002e-3;   %[Pa*s] dynamic viscosity
    muwater = 1.004e-6;   %[m^2/s] kinematic viscosity
62 rhowater = 998.2;     %[kg/m^3] density
    kappawater = 0.143e-6; %[m^2/s] thermal diffusivity
64 cpwater = 4.1813e3;   %[J/(kgK)] specific heat capacity

66 RaF=g.*alphawater.*Qj.*Lcheat^4./((rhowater*cpwater*kappawater^2*
    muwater)); % Rayleigh flux number
    Pr=cpwater*nuwater/kwater; % Prandtl number
68 F=1; % Fourier number
    tPCB=F*tboard^2*cp*rho/(kboard); % PCB characteristic time
70 fPCB=1/tPCB; % PCB characteristic frequency

72 pixelsx=xR-xL+1;
    pixelsy=yD-yU+1;
74 dx=0.15/pixelsx; % [m] x dimension of pixel
    dy=0.15/pixelsy; % [m] y dimension of pixel
76
    dt=1/4; %[s] inverse of acquired frequency [Hz]
78
%% Preallocation of different variables
80 H=pixelsy;
    W=pixelsx;
82 Thot=zeros(H,W);
    I=2:(H-1);
84 J=2:(W-1);
    T2X=0.*Thot;
    T2Y=0.*Thot;
86 [pathstr filenames extension]=fileparts(names{1,1});
88 [Gl numfr]=ReadRT(filenames,1)
    TT0=zeros(pixelsy,pixelsx);
90 TT0f=zeros(pixelsy,pixelsx,numfr);
    Thot0=size(TT0);
92 Thotm1=size(TT0);
    Thotm2=size(TT0);
94 Thot1=size(TT0);
    Thot2=size(TT0);

96 filter=fspecial('Gaussian',[7 7 7],2);
98
%% Data filtering
100 for j=1:numfr
    [Gl numfr]=ReadRT(filenames,j);
102 TT0=Gl.T(yU:yD,xL:xR);
    TT0f(:,:,j)=imfilter(TT0,filter);
104 end

106 %% Nu and h calculations
    for j=3:(numfr-2)
108 Thot0=TT0f(:,:,j);
    Thotm1=TT0f(:,:,j-1);
110 Thot1=TT0f(:,:,j+1);
    Thotm2=TT0f(:,:,j-2);
112 Thot2=TT0f(:,:,j+2);

114 T2X(I,J)=(Thot0(I,J-1)+Thot0(I,J+1)-2*Thot0(I,J))./dx^2; %

```

```

116     Second spatial derivative (x)
        T2Y(I,J)=(Thot0(I-1,J)+Thot0(I+1,J)-2*Thot0(I,J))./dy^2; %
118     Second spatial derivative (y)
        dTdt=(8.*Thot1-Thot2+Thotm2-8.*Thotm1)./(12*dt); %
    time derivative
        unsteady=rho*tboard*cp*dTdt;
118     Qk=-(kboardX*T2X+kboardY*T2Y); % [W/m^2] Conductive heat flux
        Qrad=sigma.*epsilonboard.*(Thot0.^4-Tamb.^4); % [W/m^2]
120     Radiative heat flux
        deltaT=Thot0-Tcold;
        h(:, :, j-2)=(-Qk-Qrad+Qj)./deltaT; % [W/(m^2 K)] Convective
122     heat transfer coefficient
        Nusselt(:, :, j-2)=h(:, :, j-2).*Lcheat./kwater; % [] Nusselt
        number
124 end
126 save('HC', 'Nusselt', 'h');

```

Code A.2: Heated thin foil code. Temperature evolution acquired by the camera is filtered to calculate the convective heat transfer coefficient h maps and the Nusselt number Nu maps.

```

%%%%%%%%%%%%%%%%%%%%%%%%%%%%%%%%%%%%%%%%%%%%%%%%%%%%%%%%%%%%%%%%%%%%%%%%%%
2  %                               %
%                               %
4  %                               %
%%%%%%%%%%%%%%%%%%%%%%%%%%%%%%%%%%%%%%%%%%%%%%%%%%%%%%%%%%%%%%%%%%%%%%%%%%
6
8  load('HC', 'Nusselt')
10 a=-0.25:0.5/140:0.25;
    b=0.5:0.5/140:1;
12 sec0=12;
    f=4; %Hz
14
16 for j=sec0:length(Nusselt_steady)
    t=(j-sec0)/f;
    tau=t/tc40;
18     tau=sprintf('%0.2f', tau);
    B=imrotate(Nusselt_steady(6:(end-6),6:(end-5),j),-90);
20     C=imagesc(b,a,B);
    G=get(C,'CData');
22     createfigure(G, tau)
    video(j)=getframe(gcf);
24     close all
end
26 movie2avi(video, 'transientvideo.avi');

```

Code A.3: Video code. The calculated 2D maps are rotated and named accordingly to display the desired images.

```

%%%%%%%%%%%%%%%%%%%%%%%%%%%%%%%%%%%%%%%%%%%%%%%%%%%%%%%%%%%%%%%%%%%%%%%%%%
2  %                               %
%                               %
4  %                               %
%%%%%%%%%%%%%%%%%%%%%%%%%%%%%%%%%%%%%%%%%%%%%%%%%%%%%%%%%%%%%%%%%%%%%%%%%%
6
8  function createfigure(cdata, tau)

```

```

8
% Create figure
10 figure1 = figure('Color',[1 1 1]);
    colormap('jet');
12
% Create axes
14 axes1 = axes('Parent',figure1,'YDir','normal','Layer','top',...
    'FontWeight','demi','FontSize',18,...
16 'FontName','Dutch801 Rm BT','CLim',[120 200]);
% Preserve the X-limits of the axes
18 xlim(axes1,[0.498201438848921 1.00179856115108]);
% Preserve the Y-limits of the axes
20 ylim(axes1,[-0.251798561151079 0.251798561151079]);
    box(axes1,'on');
22 hold(axes1,'all');

24 % Create image
    image([0.5:0.5/140:1],[-0.25:0.5/140:0.25],...
26 cdata,'Parent',axes1,'CDataMapping','scaled');

28 % Create xlabel
    xlabel('x/L','Interpreter','latex','FontSize',22);
30
% Create ylabel
32 ylabel('y/L','Interpreter','latex','FontSize',22);

34 % Create title
    title('Nu','Interpreter','latex','FontSize',24);
36

% Create colorbar
38 colorbar('peer',axes1,'FontWeight','demi','FontSize',18,...
    'FontName','Dutch801 Rm BT');
40

% Create rectangle
42 annotation(figure1,'rectangle',...
    [0.151 0.494 0.63 0.0820399113082042],...
44 'FaceColor',[0 0 0]);

46 % Create text
    annotation(figure1,'textbox',...
48 [0.145 0.915 0.15 0.0616740088105756],...
    'String',{'\tau = ' num2str(tau) },...
50 'FitBoxToText','off',...
    'LineStyle','none',...
52 'EdgeColor','none');

```

Code A.4: Figure code. Code showing the commands to create the images that make up the video.

Appendix B

Project budget

MATERIALS			
Article	Quantity	Price (€)	Total (€)
Electric circuit			
Power supplier (35V 215W)	1	20	20
Pack of electric cables and connectors	1	21	21
Total			41
Water circuit			
Renault Super 5's radiator-fan assembly	1	32	32
Water bucket	1	20	20
Pack of hoses and clamps	1	60	60
Power supplier(12V 120W)	1	38	38
Varistor (150 V)	1	1	1
Connector (2.1 mm)	1	1	1
Total			152
Rest of components			
* Box assembly	1	2000	200
* Black body	1	10000	500
* Infrared camera	1	50000	5000
* Computer	1	300	30
Infrared thermometer	1	20	20
Profiles (several components)	1	552	552
First surface mirror	1	58	58
Total			6310
Software			
Windows XP license	1	120	120
Matlab license (Student version)	1	35	35
Total			155
TOTAL			6658

Table B.1: Cost of materials. The cost of the products with an asterisk * is calculated according to Table B.2. A final maintenance cost of all the materials is included in the sum-up of all costs, estimated to be a 10 % of the total material's costs.

In this section all the costs related to the project are shown, including both materials and engineering work. The first ones can be seen in Table B and the second ones in Table B.3. The amortization cost of some products is shown in Table B.2, calculated according to Equation B.1.

For those products in Table B that were bought before and used for a limited time or that are going to be used later in time (usually the most expensive products), their cost is the amortization cost, calculated as Equation B.1, where A is the period of time the product has been used, B is the devaluation period of time of the product, C is the total cost of the product and D is the dedication of the product. These values are shown in Table B.2 for each product with an asterisk *.

$$Cost = \frac{A \cdot C \cdot D}{B} \quad (B.1)$$

Product	A	B	C	D	Amortization cost
Box assembly	6	60	2000	100	200
Black body	3	60	10000	100	500
Infrared camera	6	60	50000	100	5000
Computer	6	60	300	100	30

Table B.2: Amortization cost. According to Equation B.1: A is the time the product has been used (months), B is the depreciation time (months), C is the cost of the product (euros €) and D is the dedication (as a percentage %).

The cost of engineer work can be seen in Table B.3, where all activities related to the work the engineers perform are included.

ENGINEER WORK			
Operation	Hours	Price/hour (€/h)	Total (€)
Experimental activity			
Assembly of the set-up	80	25	2000
Calibration of IR camera	25	25	625
Experiments	34	25	850
Total			3875
Processing of the results			
Data acquisition	35	25	875
Report	150	25	3750
Total			4625
Others			
Displacemet expenses	40	7.5	300
Total			300
TOTAL			8800

Table B.3: Cost of engineer work.

It can be seen in Table B.4 that the total cost of the project is 14148.6 €, including the maintenance of the products within the 6 months of the duration of the experiments.

TOTAL COST €	
Materials	6658
Maintenance	666
Engineer work	8800
TOTAL	16124

Table B.4: Total project cost.

Bibliography

- T Astarita, G Cardone, and GM Carlomagno. Infrared thermography: An optical method in heat transfer and fluid flow visualisation. *Optics and lasers in engineering*, 44(3):261–281, 2006.
- Tommaso Astarita and Giovanni Maria Carlomagno. *Infrared Thermography for Thermo-fluid-dynamics*. Springer Science & Business Media, 2012.
- IEC BIPM, ISO IFCC, and IUPAP IuPAC. Oiml, guide to the expression of uncertainty in measurement. *International Organization for Standardization, Geneva. ISBN*, pages 92–67, 1995.
- G Ceglia, S Discetti, T Astarita, and GM Carlomagno. An experimental analysis in horizontal convection with ir thermography. 2012.
- S Chiu-Webster, EJ Hinch, and JR Lister. Very viscous horizontal convection. *Journal of Fluid Mechanics*, 611:395–426, 2008.
- Flir. Sc4000 datasheet, 2008. <http://www.flir.com/thermography/americas/us/content/?id=18354>.
- fsm. First surface mirror, 2015. <http://firstsurfacemirror.com/>.
- Bishakhdata Gayen, Ross W Griffiths, Graham O Hughes, and Juan A Saenz. Energetics of horizontal convection. *Journal of Fluid Mechanics*, 716:R10, 2013.
- Bishakhdata Gayen, Ross W. Griffiths, and Graham O. Hughes. Stability transitions and turbulence in horizontal convection. *Journal of Fluid Mechanics*, 751:698–724, 7 2014. ISSN 1469-7645. doi: 10.1017/jfm.2014.302. URL http://journals.cambridge.org/article_S0022112014003024.
- HJJ Gramberg, PD Howell, and JR Ockendon. Convection by a horizontal thermal gradient. *Journal of Fluid Mechanics*, 586:41–57, 2007.
- Carlo Salvatore Greco, Andrea Ianiro, and Gennaro Cardone. Time and phase average heat transfer in single and twin circular synthetic impinging air jets. *International Journal of Heat and Mass Transfer*, 73:776–788, 2014.
- Ross W Griffiths, Graham O Hughes, and Bishakhdata Gayen. Horizontal convection dynamics: insights from transient adjustment. *Journal of Fluid Mechanics*, 726:559–595, 2013.
- Harry H Hess. History of ocean basins. *Petrologic studies*, 4:599–620, 1962.

- Rui Xin Huang. Mixing and energetics of the oceanic thermohaline circulation*. *Journal of Physical Oceanography*, 29(4):727–746, 1999.
- Graham O Hughes and Ross W Griffiths. Horizontal convection. *Annu. Rev. Fluid Mech.*, 40:185–208, 2008.
- Frank P Incropera. *Introduction to heat transfer*. John Wiley & Sons, 2011.
- Harold Jeffreys. On the formation of water waves by wind. *Proceedings of the Royal Society of London. Series A, Containing Papers of a Mathematical and Physical Character*, pages 189–206, 1925.
- John Marshall and Kevin Speer. Closure of the meridional overturning circulation through southern ocean upwelling. *Nature Geoscience*, 5(3):171–180, 2012.
- Richard Charles Miller. A thermally convecting fluid heated non-uniformly from below. Master’s thesis, Massachusetts Institute of Technology, 1968.
- Julia C Mullarney, Ross W Griffiths, and Graham O Hughes. Convection driven by differential heating at a horizontal boundary. *Journal of Fluid Mechanics*, 516:181–209, 2004.
- Walter Munk and Carl Wunsch. Abyssal recipes ii: energetics of tidal and wind mixing. *Deep Sea Research Part I: Oceanographic Research Papers*, 45(12):1977–2010, 1998.
- NOAA. The motion of the ocean, 2012. <http://physics.ucsd.edu/do-the-math/2012/01/the-motion-of-the-ocean/>.
- F Paparella and WR Young. Horizontal convection is non-turbulent. *Journal of Fluid Mechanics*, 466:205–214, 2002.
- HT Rossby. On thermal convection driven by non-uniform heating from below: an experimental study. In *Deep Sea Research and Oceanographic Abstracts*, volume 12, pages 9–16. Elsevier, 1965.
- T Rossby. Numerical experiments with a fluid heated non-uniformly from below. *Tellus A*, 50(2):242–257, 1998.
- Johan Wilhelm Sandström. Dynamische versuche mit meerwasser. *Ann. Hydrodynam. Marine Meteorol*, 36:6–23, 1908.
- JW Sandström. Meteorologische studien schwedischen hochgebirge. 1916.
- William S Saric. Görtler vortices. *Annual Review of Fluid Mechanics*, 26(1):379–409, 1994.
- Henry Stommel. On the smallness of sinking regions in the ocean. *Proceedings of the National Academy of Sciences of the United States of America*, 48(5):766, 1962.
- Wei Wang and Rui Xin Huang. An experimental study on thermal circulation driven by horizontal differential heating. *Journal of Fluid Mechanics*, 540:49–73, 2005.
- Carl Wunsch and Raffaele Ferrari. Vertical mixing, energy, and the general circulation of the oceans. *Annu. Rev. Fluid Mech.*, 36:281–314, 2004.